Universidad de La Laguna

TRABAJO FIN DE GRADO

Study of the optical properties of different crystals doped with neodymium luminescent ions under extreme conditions of temperature and pressure

---

Author:
María Guillermo Cabrera

Tutors:
Dr. Víctor Lavín della Ventura
Dr. Ulises Ruymán Rodríguez Mendoza

June 2020

TABLE OF CONTENTS

ABSTRACT

A characterization of the optical properties of three crystalline lutetium garnets doped with trivalent neodymium Nd^{3+} luminescent ions has been carried out. For this purpose, steady-state optical spectroscopy has been used to measure the absorption and luminescence spectra, as well as time-resolved spectroscopy to calculate the lifetimes of the excited states of the Nd^{3+} ions in $Lu_3(Ga_xAl_{1-x})_5O_{12}$ garnets. It has also been measured how the luminescence changes with temperature, in order to calibrate a low-temperature optical sensor. Furthermore, an experimental equipment has been developed to determine the pressure in the sample's chamber of a diamond anvil cell.

1. INTRODUCTION

Spectroscopy is a field of physics dedicated to the study of the interaction between radiation and matter. More precisely, it is responsible for explaining the phenomena of absorption, emission, reflection and scattering that can take place in a material when it is exposed to certain conditions. Once a material has been studied through spectroscopic techniques, it is possible to know more information about its internal structure, temperature or composition. A fundamental magnitude in spectroscopy is the wavelength λ, which is related to the frequency ν. This magnitude is used to characterize the absorbed or emitted radiation according to the electromagnetic spectrum. This spectrum is divided into seven regions depending on the wavelength of the radiation: radio, microwave, infrared, visible, ultraviolet, X-rays and gamma rays (in order of highest to lowest wavelength). The combination of infrared, visible and ultraviolet radiation (IR-Vis-UV) is also known as optical radiation.

Depending on the type of radiation involved, it will be necessary to use different techniques to detect what is happening in the material. In the development of this work, the techniques that will be used are optical spectroscopy techniques, as this is the range of work in which the study will be carried out. These techniques basically consist on focusing a beam of light on the sample and placing a detector at the output. In this way, it can be compared the light at the entrance with the light at the exit of the sample and, therefore, it can be studied how the sample has interacted with the incident light. The result of the measurement is obtained as a spectrum, which shows how the intensity of the light changes as a function of wavelength.

Crystalline materials, or samples, that are going to be analysed are garnets doped with 1 wt% of trivalent neodymium Nd^{3+} ions. The chemical formula of each of them are $Nd{:}\,Lu_3Ga_3Al_2O_{12}$, $Nd{:}\,Lu_3Al_5O_{12}$ and $Nd{:}\,Lu_3Ga_5O_{12}$, although for convenience of reference the names $LuAGG$, $LuAG$ and $LuGG$, respectively, will be used, where G stands for "garnet". Garnets are widely used materials in optical spectroscopy as active medium for solid state lasers. The most well-known of this type of laser is the Nd:YAG (yttrium aluminium garnet) laser, whose characteristic emission is at a wavelength of $1064\ nm$. This device is what is known as a 4-level laser and is used not only in physics but also in other fields such as medicine or the industry [1-3].

It is also useful to study what takes place when the materials are exposed to conditions different from ambient ones (20 ºC and 1 atm), as there are many physical systems in which this requirement is not satisfied. The high pressure technique provides scientists with a powerful method of tuning in a controllable and reversible manner the volume of a sample and, hence, its properties. In this sense, one of its most fundamental goals is to reproduce processes similar to those occurring in the interior of the earth and other planetary objects, but it has also allowed the growth of novel applications in diverse technological areas, from materials science to food technology [4].

High pressure can be exerted on the material with the help of opposed sapphire, moissanite or diamond anvil cells, in which a hole in a pre-indented gasket forms the hydrostatic sample chamber. The determination of the pressure and temperature inside the chamber requires a previous calibration. Thanks to the transparency of the anvils to visible light, it is quite common to know the working pressure (P) and temperature (T) through an in-situ, indirect measurement of the P-T sensitive luminescence of an optically active ion.

2. AIM OF THIS WORK

The aim of this work is to study the optical properties of three garnets doped with trivalent neodymium ions. For this purpose, different optical spectroscopy techniques will be used to carry out an accurate characterization.

First, the absorption spectrum of each sample will be measured to know at which wavelengths the samples are capable of absorbing radiation. A peak or band will appear in the absorption spectrum in those wavelengths in which the energy given is resonant with an electronic transition between two levels of the Nd^{3+} ion. At room temperature, or below, the starting level is the ground state that, in the case of Nd^{3+} ions, is the $^4I_{9/2}$ multiplet. Once this information is known, the luminescence of the samples will be measured. To do this, the samples must be excited resonantly to the absorption bands in order to promote the Nd^{3+} ions to an excited state. The excited Nd^{3+} ions then relax to the ground state emitting photons, interacting with the vibrational network of the crystalline structure or transferring energy to other ions. The optical spectroscopy is focused on the emission of photons, although the other processes can be also analysed with this technique.

Thirdly, the lifetime of the emitting levels of each sample will be determined. This can be done by exciting the sample with light at a wavelength at which it absorbs and measuring how it decays from the excited state to the ground state by the emission of photons. The dynamics of this de-excitation with time is shown as a luminescence decay curve.

Finally, the luminescence measurements will be repeated but under different external conditions: low temperatures and high pressures.

3. THEORETICAL BACKGROUND

3.1. Lanthanide's atomic structure

Lanthanides comprise a group of 15 elements of the periodic table with atomic number Z between 57 and 71 and, along with scandium ($Z = 21$) and yttrium ($Z = 39$), are known as the rare-earth elements (Fig. 1). Lanthanides have similar chemical properties, while their physical properties are very different to each other and depend, to a greater extent, on the electronic configuration of the element.

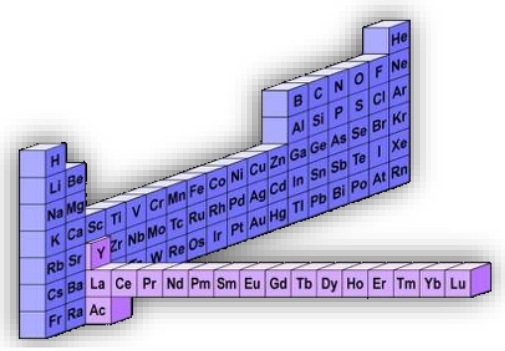

Fig. 1. Lanthanide elements in the periodic table.

The lanthanide chosen for doping the samples has been neodymium (Nd), whose electronic configuration is $[Xe]\ 4f^4\ 6s^2$, i.e. that of the xenon plus some electrons in the outer f and s shells. However, it has been used in its form as trivalent ion Nd^{3+}, which is the most stable oxidation state of this element and has a $[Xe]\ 4f^3$ electronic configuration. In this case, the electrons that occupy the $4f$ shell, which is not completely filled, are shielded by the electrons of the outer filled $5d$ shell. This confers Nd^{3+} paramagnetic properties and the capacity of interacting with radiation in the optical range (UV-Vis-IR).

In order to study the energy level structure of Nd^{3+} ion, it is necessary to consider the quantum atomic theory, since the $4f^3$ ground configuration will suffer a breakdown in its degeneracy due to the inter-electronic and spin-orbit interactions. Furthermore, once these Nd^{3+} ions are inserted in the crystal as dopants, another interaction known as crystal-field interaction must be taken into account, as a consequence of the interaction of Nd^{3+} ions with the valence electrons of the nearest neighbors atoms [5] [6].

3.2. Quantum characterization of the energy levels of lanthanide ions

Lanthanide ions interact with their environment in such a way that the energy levels can be obtained by considering the ions as free particles. However, it is also necessary to take into consideration the fine structure effects of the ion's environment in the solid. In addition, the fact that the materials are doped with low concentrations of the ion makes it possible to consider that the ions are far enough away from each other, so that there is no interaction between them.

Free-ion Hamiltonian term

A first approach to the Hamiltonian that describes the system, without taking into account external fields, is given by the contribution of four terms. For the case of an ion with N electrons

and a point nucleus of infinite mass, the Hamiltonian of the free ion in atomic units has the following structure [6]:

$$H = H_0 + H_C + H_{SO} = -\sum_i^N \frac{h^2}{2m}\nabla_i^2 - \sum_i^N \frac{Ze^2}{r_i} + \sum_{i<j}^N \frac{e^2}{r_{ij}} + \sum_i^N \xi(r_i)\vec{l}_i\,\vec{s}_i \qquad (1)$$

The first two terms of the Hamiltonian represent the kinetic and potential energies and do not affect the level structure of the system, as they contribute in the same way to all of them. On the other hand, H_C, given by the third term, is known as the Coulomb term and describes the repulsion between pairs of electrons, and H_{SO} is the spin-orbit term and represents the interaction between the spin $\vec{s_i}$ and the angular momentum $\vec{l_i}$ of the electrons.

Since the primary interest lies in the electrons contained in the $4f$ incomplete shell of the lanthanide ion, the Schrödinger equation $H\Psi = E\Psi$ is solved using the central field approximation. This assumption proposes that each electron of the incomplete $4f$ shell moves independently of the others in a field constituted by the contribution of the field created by the nucleus and a central field with spherical symmetry, which is an average potential of the electrons of the filled shells and the $4f$ electrons. In this way, it is possible to rewrite the Hamiltonian by considering only the electrons of the $4f$ shell, since the remaining electrons only contribute to a global shift of the configuration [7].

Considering that N' is the number of electrons in the $4f$ shell and $U(r_i)$ is the central potential, the Hamiltonian can be written as:

$$H' = \sum_i^{N'}\left[-\frac{h^2}{2m}\nabla_i^2 + U(r_i)\right] + \sum_{i<j}^{N'}\frac{e^2}{r_{ij}} + \sum_i^{N'}\xi(r_i)\vec{l}_i\,\vec{s}_i \qquad (2)$$

The electrostatic interaction between the $4f$ electrons causes the breakdown of the $4f^3$ configuration into a term, characterized by the ${}^{2S+1}L$ notation, that depends on the total angular momentum L and the total spin S.

The spin-orbit term characterizes a relativistic effect that is a consequence of the interaction of the magnetic spin moments of the $4f$ electrons with the magnetic field associated with their radial motion. This effect causes a splitting of the energy levels that leads to a partial breakdown of the degeneration. As a result, states, also known as multiplets, characterized by the ${}^{2S+1}L_J$ notation, are obtained. Through quantum mechanics, it is known that there are $2J+1$ states with the same energy [6]. In the case of lanthanide ions, the magnitude of the spin-orbit effect is comparable to the electrostatic interaction. Therefore, it can be said that the LS or Russell-Saunders coupling has been broken and the new situation is known as intermediate coupling, in which J is the total angular momentum and is a good quantum number.

Crystal-field Hamiltonian term

Crystal-field theory describes the splitting of energy levels of the lanthanide ions as a consequence of their interaction with their nearest ligands in a solid. Ligands are ions or molecules that are attached by a chemical bond to the $4f$ electrons through the sharing of one or more pairs of electrons and that together form a coordination complex. They include molecular groups such as $O^{2-}, OH^{-}, {SO_4}^{2-}$, etc. This theory was developed by Hans Bethe [8] and John Hasbrouck Van Vleck [9] in the 1930s. The interaction that takes place between the ion, which is actually a cation, and the ligands has an electrostatic origin. The ion is positively charged and it is attracted by the negative charge of the valence electrons of the ligands. However, these electrons cause the electrons in the $4f$ orbitals of the cation to repel each other. As a consequence, the $4f$ orbitals, which were previously degenerated in energy, are split according to the strength of the ion-ligand bond.

The $4f$ shell of the lanthanide ions does not have spherical symmetry. This implies that its shape and occupation, i.e. the point symmetry of the lanthanide-ligands first coordination shell, play an important role in the interaction with the ligands. In addition, this model takes the assumption that ligands are point charges located in certain positions in space. Therefore, the repulsion between the electrons of the ion and the ligands will not be the same in every case, since it will depend on the distance and direction of the bonds that connect them. Because of this, there will be a breakdown of the degeneracy of the ${}^{2S+1}L_J$ multiplets, known as crystal-field splitting, which generates new energy levels [10]. It is worth noting that the magnitude of the crystal-field interaction is smaller than the electrostatic and spin-orbit ones.

The crystal-field splitting will depend on various factors such as the nature of the ion and the ligands bonds, the oxidation state of the ion and the spatial geometric configuration, i.e. the local point symmetry, between the ligands and the ion. Since the result of the splitting of levels is similar to the one produced by the Stark effect, the resulted energy levels are commonly known as Stark levels. The occupation of the electrons in the split orbitals is ruled by *Pauli's exclusion principle* and *Hund's rule*. According to this, if an electron is added, it will have the possibility to fill an orbit with higher energy or to complete one that is already half-filled. Whether one or the other occurs will depend on the pairing energy δ and the crystal-field splitting energy gap ΔE:

Firstly, strong-field ligands are those that cause the energy gap between higher and lower energy orbitals to be greater than the pairing energy of the electrons ($\Delta E > \delta$). In this case, the half-filled orbitals of lower energy will be filled before the ones of higher energy. These types of complexes are known as low-spin complexes, since the sum of magnetic moments due to the electrons is the minimum possible.

On the other hand, if $\delta > \Delta E$, the ligands are called weak-field ligands and it is more energetically efficient for the system to complete the higher energy orbitals. The complexes in which this occurs are called high-spin complexes and their sum of magnetic moments is the maximum possible. This is the case of lanthanide ions.

Through this information, it is possible to study the magnetic properties of a material. Moreover, if in the energy level diagram there are electrons with unpaired spins, the complex will be paramagnetic and will be attracted by magnetic fields. On the other hand, if it does not have unpaired electrons, it will be a diamagnetic complex and, therefore, it will be weakly repelled by the magnetic fields. Lanthanide ions are paramagnetic.

The term that must be added to the Hamiltonian in order to take into account the crystal-field interaction is given by [11]:

$$H_{CF} = \sum_i eV(r_i, \theta_i, \phi_i) \tag{3}$$

where $eV(r_i, \theta_i, \phi_i)$ is the potential generated by the environment at position (r_i, θ_i, ϕ_i) for the *i-th* valence electron.

Other Hamiltonian terms

It should be pointed out that, apart from the contributions mentioned, there are other interactions whose order of magnitude in lanthanide elements is generally significantly lower than these ones and can be neglected. Among them, there can be found relativistic magnetic interactions such as spin-spin interaction. They contribute to the energy of the whole $4f^3$ configuration, but not to the breakdown of the degeneracy.

In garnet crystals, the energy levels that will be studied deeply are those corresponding to the $^4F_{3/2}$ and $^4I_{9/2}$ multiplets, which are split respectively into two and five Stark energy levels (see Fig. 2), respectively, due to the low point symmetry of the Nd^{3+} site in the crystal.

3.3. Crystalline structure of garnet crystals

A space group is a symmetrical group that has a certain structure in space. In the case of working in a 3-dimensional space, the groups are called Fedorov groups or crystallographic groups and describe the symmetry of the crystal, whose crystallographic structure can be determined by X-ray diffraction techniques. There exist 230 different crystallographic groups [12].

Oxide garnets have the general formula $A_3B_2C_3O_{12}$. For the lutetium gallium/aluminium garnet, $Lu_3(Ga_xAl_{1-x})_5O_{12}$, A atoms correspond to lutetium (Lu) while B and C atoms correspond to gallium (Ga) and aluminium (Al). $LuAGG$ crystallizes in the body-centered cubic (bcc) structure (space group Ia-3d, No. 230, $Z = 8$) and has 160 atoms in the conventional unit cell (80 in the primitive cell). Ga and Al atoms in the formula unit occupy octahedral sites of S_6 and S_4 symmetries. The Lu^{3+} ions (or substitutional Nd^{3+} ones) are placed in dodecahedral sites. The garnet structure can be seen as a network of LuO_8 dodecahedra, GaO_6 octahedra and GaO_4 tetrahedra interconnected with shared O atoms at the corners (see Fig. 3 left) [13].

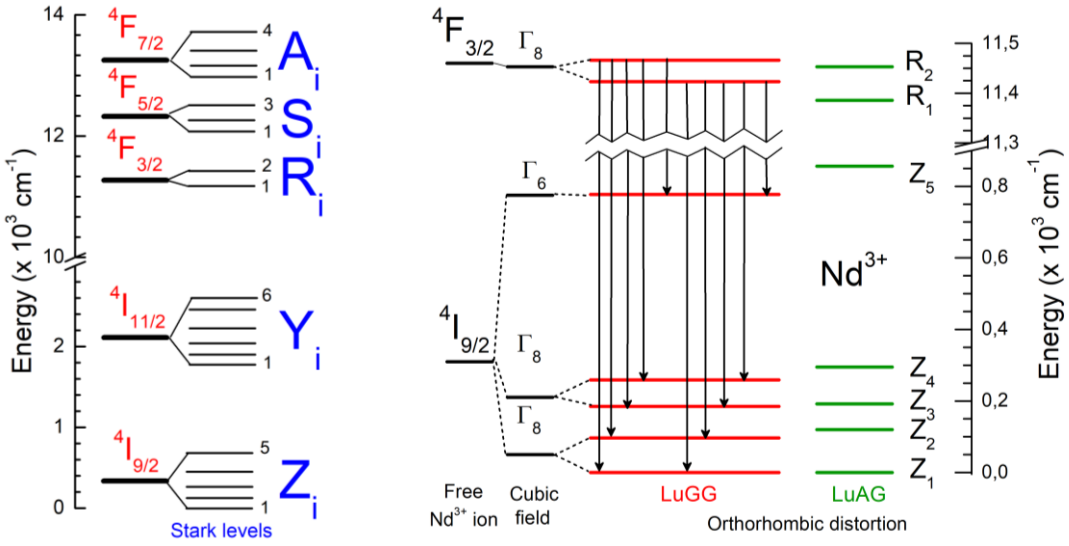

Fig. 2. (Left) Partial energy level diagram of the Nd^{3+} ion in a solid. Free-ion $^{2S+1}L_J$ multiplets and the Stark levels are shown. (Right) Energy level diagram of the split $^4F_{3/2}$ and $^4I_{9/2}$ levels due to the crystal-field interaction for $LuGG$ and $LuAG$ crystals.

The LuO_8 dodecahedra has a D_2 local point symmetry, i.e. taking the Lu^{3+}, or the Nd^{3+}, ions at the origin of an orthogonal reference system, the distances and angles of the bonds between each central ion and the eight surrounding oxygen ions form an orthorhombic environment with D_2 symmetry (Fig. 3 right). In other words, the electronic interaction between the Lu^{3+} (or Nd^{3+}) central ion and the surrounding ligands, known as the crystal-field interaction, shows the same crystallographic symmetry of the local point symmetry of the central ion.

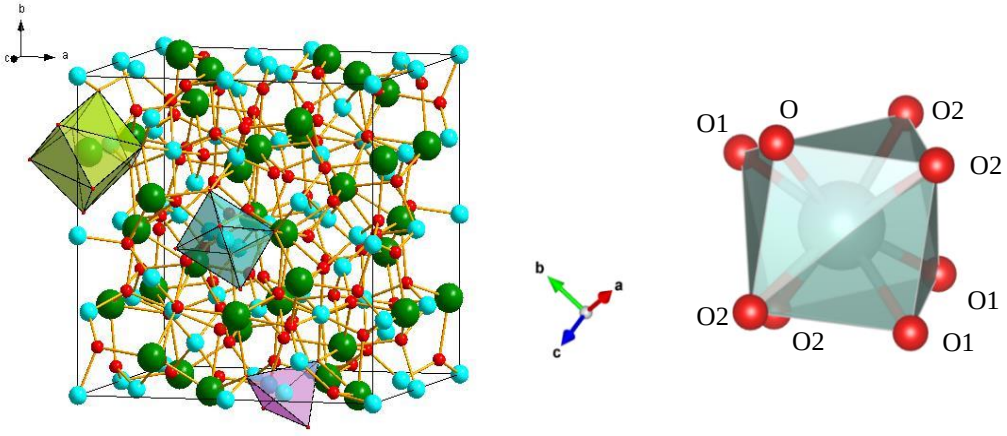

Fig. 3. (Left) Unit cell of the $Lu_3(Ga_xAl_{1-x})_5O_{12}$ garnet structure. The LuO_8 dodecahedron (green), GaO_6 octahedron (blue) and GaO_4 tetrahedron (pink) polyhedra are highlighted. Green spheres represent the Lu atoms, blue spheres correspond to the Ga atoms, and the small red spheres to the O atoms. (Right) NdO_8 polyhedron.

However, for low symmetry sites, such as those found for Lu^{3+} or Nd^{3+} ions in garnets, it is often convenient to describe the effect of the crystal-field as a deformation or distortion of a main cubic symmetry [14] [15]. Thus, the D_2 crystal-field interaction in $LuAGG$ garnet between the Lu^{3+} and the Nd^{3+} ions and the eight surrounding oxygen ions can be described as a pure

cubic symmetry component with a superimposed non-cubic symmetry component that accounts for the true D_2 symmetry at the Lu^{3+} and Nd^{3+} sites [16]. This information is of paramount importance to understand the optical properties of the lanthanide ions in the garnets, since the crystal-field interaction rules the energy level diagram and the transition probabilities between them.

3.4. Lambert-Beer's law and oscillator strength

Lambert-Beer's law is an empirical law that characterizes the absorption of radiation of a sample. The law states that when a light beam of intensity $I(\lambda)$ enters a sample a distance x, the intensity decreases as a function of the travelled distance and the intensity of the radiation as follows:

$$\frac{dI(\lambda)}{dx} = -\alpha(\lambda)I(\lambda) \tag{4}$$

The parameter $\alpha(\lambda)$ $[cm^{-1}]$ is known as the absorption coefficient and depends on the wavelength of the radiation. It can be expressed as:

$$\alpha(\lambda) = \sigma(\lambda)\, N \tag{5}$$

where $\sigma(\lambda)$ $[cm^2]$ is the absorption cross-section and N $[cm^{-3}]$ is the concentration of ions.

If the differential equation of the Lambert-Beer's law is solved, it can be seen that the decay of the radiation intensity is exponential, decreasing as the radiation penetrates deeper into the material:

$$I(\lambda) = I_0(\lambda)e^{-\sigma(\lambda)Nx} \tag{6}$$

where $I_0(\lambda)$ is the amount of radiation right on the surface of the material.

If in the previous expression decimal logarithms are taken, a dimensionless physical quantity known as absorbance $A(\lambda)$ can be obtained. In addition, the optical density, OD, that represents the absorption of the sample as a function of the wavelength of the radiation can be also calculated:

$$A(\lambda) = \log\left(\frac{I_0(\lambda)}{I(\lambda)}\right) = \frac{\sigma(\lambda)\, N\, x}{2.303} \tag{7}$$

$$OD = -log\left(\frac{I(\lambda)}{I_0(\lambda)}\right) = -\log\left(e^{-\sigma(\lambda)Nx}\right) = \frac{\sigma N}{2.303}x \tag{8}$$

On the other hand, through a mathematical analysis, it can be concluded that integrating the absorption coefficient $\alpha(\lambda)$ in each of the absorption peaks corresponds to analyzing the transition probability from a state i (generally, the fundamental state) to an excited state f. This

probability is related to the Einstein coefficients A_{if} for the induced absorption of each of the transitions. From these coefficients, another parameter known as oscillator strength f can be obtained. It represents the ratio between the real absorption probability and the absorption probability for an electron moving in a three-dimensional isotropic harmonic oscillator with a frequency equal to the resonance one [17].

The general procedure used to obtain the experimental oscillator strengths of a transition from the ground state J to an excited J' is to use the Smakula's expression [18]:

$$f_{exp}\,(aJ, bJ') = \frac{mc^2}{\pi e^2 N d} \cdot \frac{n^2}{\chi} \int \frac{2.303\; OD(\lambda)}{\lambda^2}\, d\lambda \tag{9}$$

where m and e are the mass and charge of the electron, c is the speed of light, $N\ [cm^{-3}]$ is the ion concentration, $d\ [cm]$ is the thickness of the sample, $OD(\lambda)$ is the optical density at the wavelength λ and χ is the correction factor for the refractive index of the matrix.

The oscillator strength can also be given considering two contributions concerning the magnetic and electric dipolar character of the transitions, since multipoles of higher orders are generally neglected [19]:

$$f = f_{ED} + f_{MD} \tag{10}$$

The electric dipole term was modelled by B. R. Judd [20] and G. S. Ofelt [21] through the sum of the intensities due to each of the components of the crystal-field interaction of a certain quantum state, and it was condensed in the so called Judd-Ofelt theory. Considering n as the refractive index of the medium and $\bar{\lambda}$ as the average wavelength of the band, the oscillator strength corresponding to the transition from a state a with total angular momentum J to an excited state b with total angular momentum J' can be theoretically written as [19] [22]:

$$f = \frac{8\pi^2 mc}{3he^2\bar{\lambda}(2J+1)}\left[\chi f_{ED}(aJ, bJ') + n f_{MD}(aJ, bJ')\right] \tag{11}$$

where

$$\chi = \frac{(n^2+2)^2}{9n} \tag{12}$$

$$f_{ED}(aJ, bJ') = e^2 \sum_{i=2,4,6} \Omega_i \left|\langle aJ|\, U^{(i)} |bJ'\rangle\right|^2 \tag{13}$$

$$f_{MD}(aJ, bJ') = \left(\frac{e}{2mc}\right)^2 \left|\langle aJ|\vec{L} + 2\vec{S}|bJ'\rangle\right|^2 \tag{14}$$

being Ω_i the Judd-Ofelt parameters, $U^{(i)}$ an unit tensor of rank i, $\vec{L}$ the angular momentum operator and $\vec{S}$ the spin operator.

If the only term considered is that of the electric dipole, the measured line oscillator strength S_m $[cm^2]$ can be obtained through the following expression:

$$S_m = \frac{3hc(2J+1)}{8\pi^3 e^2 \chi\, \bar{\lambda}\, N} \int \alpha(\lambda)\, d\lambda \tag{15}$$

The theoretical value of this magnitude is related to the Judd-Ofelt parameters through Eq. (16). These parameters can be obtained by means of a least-squares fitting in which the difference between the experimental and calculated values has to be the least possible.

$$S_{cal} = \sum_{i=2,4,6} \Omega_i \left|\left\langle U^{(i)} \right\rangle\right|^2 \tag{16}$$

There is another parameter known as quality factor X that characterizes the spectroscopic quality [23] and corresponds to:

$$X = \frac{\Omega_4}{\Omega_6} \tag{17}$$

3.5. De-excitation of electronic levels and lifetime

When an electron is placed in an excited state, it can decay to the fundamental state through two types of processes: radiative and non-radiative. Radiative processes are those in which photons are involved, either by absorption or emission. These include induced absorption, induced emission and spontaneous emission processes. This last process, which consists of the decay to a lower level of an ion that was at an excited level through the emission of a photon in any direction, is particularly relevant. The rate or probability per unit of time of this phenomenon is expressed as:

$$\frac{dP_{21}}{dt} = A_{21} \tag{18}$$

where A_{21} is Einstein's coefficient for spontaneous emission.

According to the Judd-Ofelt theory, the spontaneous transition probability A can be written as [22]:

$$A\,(aJ, bJ') = \frac{64\pi^4 n^2}{3hc^2 \bar{\lambda}^3 (2J+1)} [\chi f_{ED}(aJ, bJ') + n f_{MD}(aJ, bJ')] \tag{19}$$

If only electric dipole effects are considered, the expression can be reduced to:

$$A\,(aJ, bJ') = \frac{64\pi^4 e^2}{3hc^2 \bar{\lambda}^3 (2J+1)} \frac{n(n^2+2)^2}{9} \sum_{i=2,4,6} \Omega_i \left|\left\langle U^{(i)} \right\rangle\right|^2 \tag{20}$$

Through this magnitude, another one known as the branching ratio can be calculated as follows:

$$\beta = \frac{A(aJ, bJ')}{\sum_{bJ'} A\,(aJ, bJ')} \tag{21}$$

Either from the branching ratio or the spontaneous transition probability, the radiative lifetime of an excited state, defined as the lifetime that would be obtained if the only mechanism the level can be depopulated through is by spontaneous emission, can be determine through the following expression [22]:

$$\tau_{rad} = \frac{1}{\sum_{bJ'} A\,(aJ, bJ')} = \frac{\beta}{A(aJ, bJ')} \tag{22}$$

Nevertheless, there are many cases in which the real lifetime of an electronic level does not coincide with the radiative lifetime. This is because the lifetime decreases if depopulation is, in addition, due to the intervention of non-radiative processes. These processes produce a quenching effect, leading to a reduction in the number of photons emitted and, hence, in the intensity of the luminescence. Non-radiative processes are those in which photons are not involved. Some of the most important non-radiative processes are multiphonon de-excitation and non-radiative energy transfer.

Multiphonon de-excitation processes consist on the emission of phonons (normal modes of vibration) to the crystal lattice, which causes an increase in the temperature of the system. In the case of lanthanide ions, the probability of a multiphonon transition at a temperature T is given by Eq. (23):

$$W_{MP}(T) = W_{MP}(T = OK)\left(1 + \frac{1}{e^{h\omega/KT} - 1}\right)^{p} \tag{23}$$

where the sub-index MP refers to multiphonon de-excitation and p is the number of phonons with energy $h\omega$ transferred to the lattice. The number of phonons p can be determined through the characteristic energy gap ΔE and the frequency ω of the transition:

$$p = \frac{\Delta E}{h\omega} \tag{24}$$

following the well-known “Gap Law”.

On the other hand, the non-radiative energy transfer processes consist on the excitation of a lanthanide ion, known as acceptor, due to the de-excitation of another lanthanide one, called donor. A common example that can occur is that in which ion A is in an excited level, while ion B is in the ground state. It can happen that the energy released when ion A is de-excited to the ground state is given, or transferred, to ion B and, thanks to it, it promotes to the excited level, without the emission of photons out of the sample. The probability of this process is inversely

proportional to the distance between the two molecules R_0 raised to a power S that depends on the kind of interaction between the ions [11]:

$$W_{ET} = \frac{cte}{{R_0}^S} \tag{25}$$

although it is worth noting that it also strongly depends on the overlapping of the emission bands of ion A and the absorption bands of ion B.

Considering what has been mentioned so far, the average lifetime of an excited level can be calculated through the following expression [11]:

$$\tau = \frac{1}{A_{21} + W} \tag{26}$$

$$W = W_{MP} + W_{ET} \tag{27}$$

where A_{21} is Einstein's coefficient for spontaneous emission and W is the probability of transition that takes considers non-radiative processes. It is observed that the lifetime decreases as the probability of transition of non-radiative processes W increases. This increase can be attributed to the following contributions:

- The increase in the temperature of the lattice that causes W_{MF} to increase.

- The increase in the concentration of optically active ions leads to a decrease in the distance between them, thus increasing W_{ET}.

With the only presence of radiative and multiphonon processes, the luminescence would decay exponentially over time, meaning that, in a logarithmic representation, it is obtained a straight line with a negative slope. However, when non-radiative energy transfer processes become important, the curve is no longer adjustable to a single exponential one, especially at short times after the laser pulse excitation. In these cases, and for comparison purposes, it is useful to define an averaged lifetime τ_{exp} [25] as:

$$\tau_{exp} = \frac{\int_0^\infty t\, I(t) dt}{\int_0^\infty I(t) dt} \tag{28}$$

The Inokuti-Hirayama model

If the lifetime curves do not fit well to an exponential model, it is possible to resort to a widely used model in the area of solid-state physics known as the Inokuti-Hirayama model [26]. The model states that the intensity decays through the following expression once it is excited with a laser pulse:

$$I(t) = I_0 \exp\left[-\left(\frac{t}{\tau_0}\right) - Q\left(\frac{t}{\tau_0}\right)^{3/S}\right] \quad (29)$$

where I_0 is the initial amplitude of the intensity emitted, τ_0 the intrinsic lifetime of the donor in the absence of the acceptor, Q a dimensionless parameter that characterizes the energy transfer and S a parameter that depends on the predominating type of mechanism in the interaction. Specifically, the values that S can take are $S = 6, 8, 10$ depending on whether the dominant donor-acceptor interaction is dipole-dipole, dipole-quadrupole or quadrupole-quadrupole kind, respectively.

The Q parameter can be calculated through the expression:

$$Q = \frac{4\pi}{3}\,\Gamma\left(1 - \frac{3}{S}\right) N_O {R_0}^3 \quad (30)$$

where N_O is the concentration of acceptors and R_0 is the critical transfer distance, which corresponds to the separation distance between the donor and the acceptor for which the energy transfer rate to the acceptors is equal to the intrinsic decay rate of the donor. The value of the parameter S can be modified until the model correctly reproduces the data acquired. This allows predicting the dominating interaction between Nd^{3+} ions that causes energy transfer processes.

3.6. Luminescence Intensity Ratio (LIR) technique

The luminescence intensity ratio technique, abbreviated as LIR, is a method used to determine the temperature of a system through optical thermometry procedures and is based on changes of the luminescence intensity ratio of two close-energy emitting levels of an optically active doped sample as a function of temperature. An increase in temperature causes the population of the higher energy level to increase at the expenses of the lower level due to thermal excitation, while a decrease in temperature leads to the depopulation of the higher level and the population of the lower energy one. By studying changes with temperature in the relative intensities of the electronic transitions of a determined ion in a specific sample, it is possible to calibrate it as a temperature sensor.

The energy levels chosen for this purpose must be closely spaced in energy, as it is necessary that they are thermalized, i.e. the energy gap between levels has to be similar to the free thermal energy of the system. Thanks to this, there exists thermal equilibrium between the levels and the Boltzmann distribution can be used to characterize them [27] [28].

The LIR between two thermally coupled levels of a lanthanide ion can be expressed as the ratio between the emission intensities of each level [29] and it depends on the temperature according to the Boltzmann distribution, as already mentioned:

$$LIR = \frac{I_i}{I_j} = A \exp\left(-\frac{\Delta E}{k_B T}\right) \quad (31)$$

where ΔE is the energy gap between the two thermally coupled levels, k_B is Boltzmann's constant, T is the absolute temperature and A is a constant independent of temperature.

An important parameter when characterizing a temperature sensor is the relative sensitivity S, which represents how the LIR changes as the temperature varies. It can be expressed as [29]:

$$S[K^{-1}] = \frac{1}{LIR}\frac{dLIR}{dT} = \frac{\Delta E}{k_B T^2} \quad (32)$$

From this equation, it can be concluded that the greater the energy gap ΔE between the two thermal levels, the greater the sensitivity. Therefore, when using lanthanide ions in optical temperature sensors, it is convenient that the energy gap between levels is as high as possible. However, the pair of levels has to be chosen carefully because if the levels are too far apart, thermalization is no longer observed.

3.7. Ruby: properties and applications as pressure gauge

The development of diamond anvil cells (DAC) has contributed significantly to the scientific research on high pressures. The widespread use of these cells is justified by the simplicity with which pressure can be applied and measured. Ideally, an optical pressure sensor should have a single emission line, with no broadening or weakening, a large shift with pressure, a small temperature-dependent line shift and a small linewidth [30] [31]. The chromium trivalent ion Cr^{3+} in ruby is the most commonly used luminescence pressure sensor due to the strong $^2E \rightarrow {}^4A_2$ luminescence, its large line shift with pressure and easy excitation with commercial lasers, although its main drawback is the low-pressure sensitivity below 1 GPa, in the range of interest for life-related high pressure research [31] [32].

Ruby is one of two varieties of the corundum mineral, the other one is sapphire. It is composed of alumina (Al_2O_3) and chromium (Cr) impurities. More specifically, Cr^{3+} ions replace some of the aluminium ions Al^{3+}, forming a complete solid solution between the two oxide phases $(Al_2O_3 - Cr_2O_3)$ (see Fig. 4 left). As the ionic radius of Cr^{3+} ions is slightly larger than that of Al^{3+} ions, doping the corundum with chromium slightly increases the size of the lattice host. Thanks to X-ray diffraction experiments, it has been observed that, under hydrostatic pressure, the ruby lattice is deformed almost isotropically [33] [34]. In addition, it has also been studied the effects generated in the ruby optical transitions when applying pressure. For this purpose, the crystal-field levels of Cr^{3+} in ruby (Fig. 4 right), their degeneration and splitting factors have been analyzed.

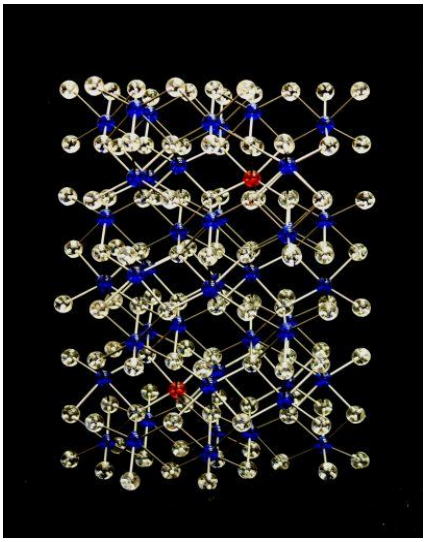

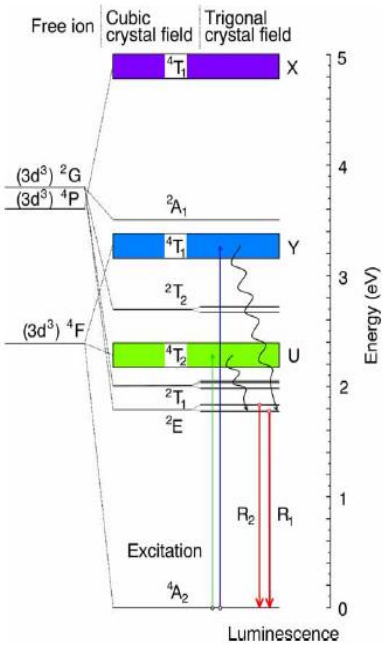

Fig. 4. (Left) Crystal structure of ruby showing the substitution of Al^{3+} ions (blue) with Cr^{3+} ones (red). (Right) Energy levels of the Cr^{3+} ion.

As it can be seen in Fig. 4 (right), there are two sharp Cr^{3+} emission lines known as R-lines (R_1 and R_2). These are the ones that will be used to measure the pressure in the DAC. As the concentration of Cr^{3+} ions in the ruby increases, the lattice parameters change and the frequency of the R-lines is also affected. Therefore, it is necessary to take into account the volume coefficient of the frequency shift associated with doping [32]:

$$\Delta\nu\ (cm^{-1}) = 660\frac{\Delta V}{V_0} \tag{33}$$

Furthermore, there is another factor that affects the frequency of the R-lines even more than the doping concentration: the temperature. As the temperature decreases, the R-lines are shifted towards shorter wavelengths (higher energies), the width of the peaks decreases and the R_2/R_1 intensity ratio decreases as well [35]. However, it is generally assumed that this effect is independent of doping and pressure. Thus, if measurements are taken at a constant temperature, the frequency shift is the same in all of them. Therefore, the total frequency shift can be expressed as a superposition of the three contributions:

$$\Delta\nu = \Delta\nu\ (c) + \Delta\nu(T) + \Delta\nu(\sigma_{ij}) \tag{34}$$

where c is the concentration in weigh percent of Cr_2O_3 and σ_{ij} represents a general symmetric stress tensor.

In order to use the ruby as an optical sensor and take pressure measurements, it must be calibrated. In general, this procedure consists of measuring the wavelength of the R-lines and,

simultaneously, the specific volume of a marker compound assumed to be exposed to the same stress conditions as the ruby, by using X-ray diffraction techniques.

When pressure is applied to the ruby, there is a shift towards longer wavelengths of the Cr^{3+} energy levels (see Fig. 5) due to an increase in the octahedral crystal-field strength. This shift is considered linear up to pressures of 20 GPa and, although there are several calibration coefficients, the original and more accepted value for the R_1 line is that obtained by Piermarini [36], which was later confirmed by Nakano [37]:

$$\left(\frac{dv}{dP}\right)_0 = -7.53\ cm^{-1}/GPa \tag{35}$$

$$\left(\frac{dP}{d\lambda}\right)_0 = 0.27\ \pm 0.01\ GPa/\text{Å} \tag{36}$$

Above 20 GPa, a substantial nonlinear component of the R-lines shift is observed. A variety of nonlinear pressure calibrations with the frequency have been proposed [32].

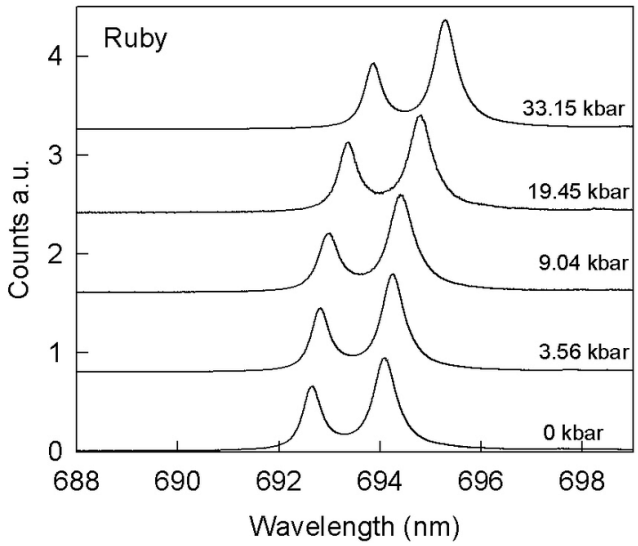

Fig. 5. Ruby luminescence under different pressures [38].

4. METHODOLOGY

4.1. Growth and preparation of samples

The lutetium gallium/aluminium garnet crystals used in this study were synthesized at the *Research Laboratory on Advanced Crystal Engineering* of the *Institute of Materials Research* (IMR, Sendai, Japan) under the supervision of Prof. Dr. Akira Yoshikawa and Prof. Dr. Kei Kamada. The synthesis of the crystals was carried out using the micro-pulling-down (μ-PD) technique. This method consists on a continuous transport of the melted material trough micro-channels made in a crucible bottom. The continuous solidification of the melt takes place in a liquid or solid

interface located under the crucible. In a steady state, both the melt and the crystal are pulled-down with a constant, but generally different, velocity [39] [40].

Before starting measuring, the samples were cut using a *Low Speed Diamond Saw* to reduce their thickness. After that, they were polished with a 1200 grain number sandpaper and also with 1 μm diamond powder until all the imperfections were corrected to an optical grade.

4.2. Ambient conditions measurements

Absorption, luminescence and lifetime measurements were taken under ambient conditions. These conditions correspond to the usual temperature and pressure in the *Laser Spectroscopy and High Pressures Laboratory* of the *University of La Laguna*, where, as a reference, $T = 22°C$ and $P = 1\ atm$ are considered.

4.2.1. Absorption

In order to obtain the absorption spectra of the different samples, it was used an *Agilent Technologies Cary* Series *UV-Vis-NIR Spectrophotometer* (Fig. 6). There were taken spectra of two wavelengths ranges: from 300 nm to 900 nm and from 1450 nm to 1800 nm, which include the ultraviolet (UV), visible (Vis) and near-infrared (NIR) range of the electromagnetic spectrum.

Fig. 6. *Agilent Technologies Cary Series UV-Vis-NIR Spectrophotometer*.

In the UV-Vis range, measurements were obtained by setting an integration time of 1 s, with a slit of 0.5 mm and a spectral resolution of 0.3 nm. While in the NIR range, the signal was lower and, as a consequence, the integration time had to be increased to 4 s and the slit was opened to 1 mm. In this case, measurements were taken every 0.5 nm. Moreover, as there was special interest in the 800 - 900 nm range, it was taken a more cautious measurement in this part, setting a longer integration time for each measurement. Concretely, it was used a 10 s integration time, a 0.6 mm slit and a spectral resolution of 0.5 nm.

4.2.2. Luminescence

The luminescence was measured using two different spectrometers: a *TRIAX 320* and an *Andor Shamrock SR-303i*. The first one was used to obtain the spectrum from 820 nm to 1700 nm. As this interval is contained in the NIR range, it was necessary to incorporate a *HAMAMATSU NIR extended photomultiplier*, set in 650 V. Apart from this, it was used a 0.15 mm slit, an integration

time of 500 ms and a spectral resolution of 0.25 nm. Moreover, the grating used had 600 groves/mm and a 1500 nm blaze.

A second spectrometer was used due to the fact that the *TRIAX 320* was not sensitive enough at shorter wavelengths. The *Andor Shamrock SR-303i* consists of a detector and a *Newton CCD Camera*. It was able to acquire the spectrum from 820 to 1200 nm, using an integration time of 2 s, a 100 µm slit, a grating with 1199 lines/mm and a blaze of 1000 nm.

In both cases, it was used a *Spectra Physics 3900S tunable Ti:sapphire laser*, tuned in 808.7 nm with a power of 200 mW, pumped by a *Millenia laser* with a power of 2.5 W, to excite the samples. Besides, it was configured a simple set-up to take the measurements: the laser emission was sent to the sample through a pair of mirrors and a converging lens, following a 90º excitation-detection configuration.

4.2.3. Lifetime

The lifetime measurements were obtained through an *Optical Parametric Oscillator OPO* (Fig. 7 left), which is a pulsed laser that emits pulses with 10 nanoseconds of duration. It was configured an emission wavelength of 808 nm. The data obtained was acquired with a *LeCroy WaveSurfer 424 200MHz Oscilloscope* (Fig. 7 right) and the *TRIAX 320* mentioned before. A 10 $k\Omega$ resistor was connected to turn the current signal into a voltage one.

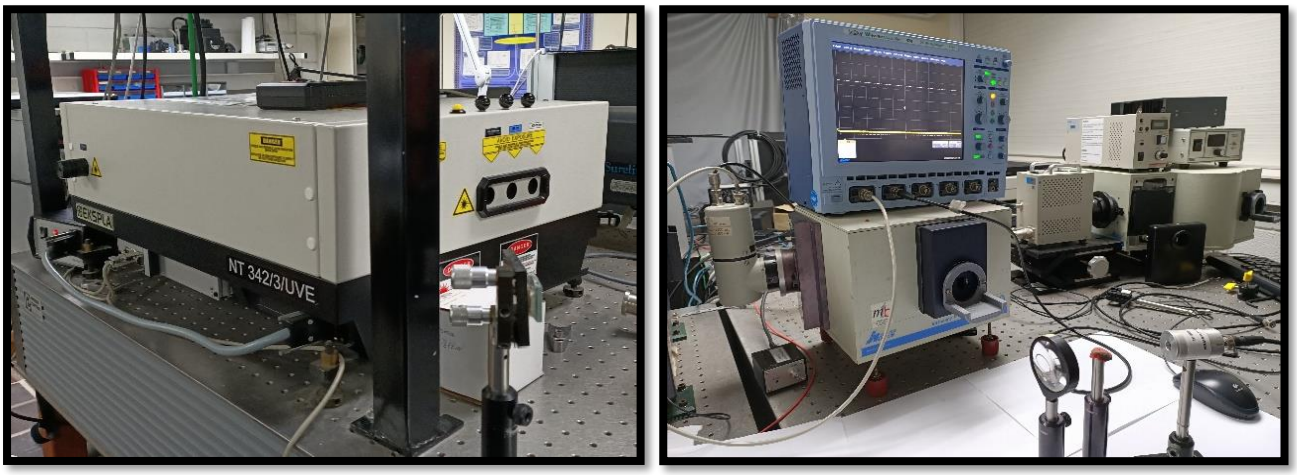

Fig. 7. (Left) *Optical Parametric Oscillator*. (Right) *LeCroy WaveSurfer Oscilloscope* and *TRIAX 320*.

4.2.4. Upconversion

A study was performed to verify if any of the three samples show upconversion processes. For this purpose, the samples were excited through the *Spectra Physics 3900S tunable Ti:sapphire laser* previously mentioned. It was tuned in 808.7 nm.

4.3. Extreme conditions measurements

4.3.1. Low temperatures

It has also been measured how the luminescence changes when the temperature of the sample varies. A cryostat and a vacuum pump (Fig. 8 left) have been used for this purpose. The combined operation of these two devices allows the temperature of the sample to be reduced to about 40 K. The sample temperature is measured by a thermocouple that is in contact with the sample through a thermal-conductive greasy paste inside the cryostat.

The experimental set-up consists of a *Spectra Physics 3900S tunable Ti:sapphire laser* (pumped by a *Millenia laser*) which, through a couple of mirrors, reaches a converging lens that is able to focus the light beam on the sample. Actually, it should not really focus perfectly because it could produce the phenomenon of dielectric breakdown in the sample, which manifests itself by emitting white light. At the output of the set-up, there is another lens that focuses the light emitted by the sample on the detector (Fig. 8 right). This emission is analyzed by the *Andor Shamrock SR-303i spectrometer* previously mentioned. The system has been set-up using a 90º excitation-detection configuration.

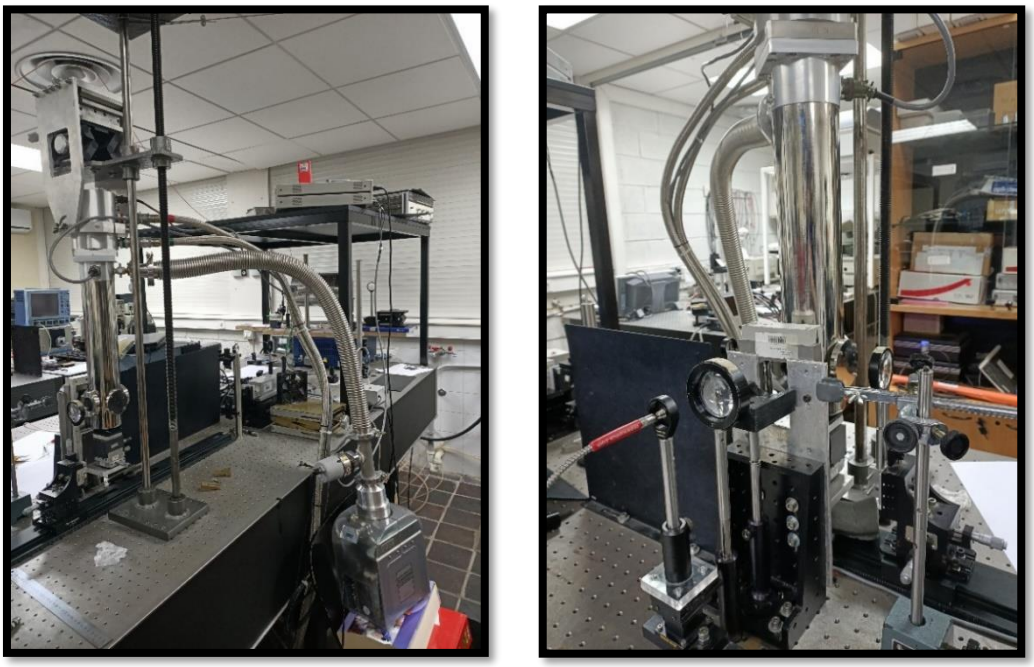

Fig. 8. (Left) Cryostat connected to a vacuum pump. (Right) Detector and lens used to measure luminescence.

In order to run the experiment, a compressor, which is the instrument responsible of cooling down the sample, is turned on. The temperature of the sample is shown in the *LakeShore Temperature Controller*. After approximately 3 hours, when it is observed that the temperature cannot drop further, measurements start being taken. The first measurement was taken at a temperature of about 40 K. Once taken, the compressor is turned off and the temperature begins to increase. Measurements were taken every 20 K until room temperature was reached.

4.3.2. High pressures

A study of luminescence under high pressure conditions was planned to be carried out. However, given the special circumstances of this academic year, it was only possible to start it and to develop a new instrument dedicated to high pressure measurements.

Nowadays, one of the most used techniques to confer high pressures to a sample is the use of a diamond anvil cell (DAC). This system consists of two 16-sided diamonds placed on a metal support whose faces are facing each other (see Fig. 9).. These faces, known as culets, must be perfectly parallel, otherwise the pressure on the sample will not be uniform. High pressures can be achieved with this system due to the section on which the force is applied is very small. Specifically, the culet diameter is about 400 µm.

On the other hand, a metallic gasket of about 200 µm must be placed between the diamonds. Its function is to avoid that, due to a mechanical failure, the diamond faces could touch each other. The diamond-to-diamond pressure could cause one or both of the diamonds to break. The gasket used (Fig. 10 left), which is made of tungsten carbide, has a previous preparation as it needs to have an orifice in which the sample, the ruby ball and the pressure transmitter fluid are placed. First, it is inserted between the two diamonds and the cell is closed in such a way that the pressure applied is the minimum for which the screws that hold both parts of the cell are not loose.

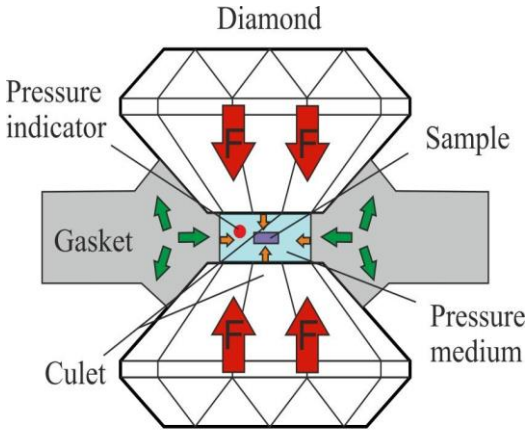

Fig. 9. Schematic sketch of a diamond anvil cell [41].

Once this is done, a *Heidenhain ND221B* length gauge (Fig. 10 centre) with a resolution of 0.5 µm is used to set a thickness of 200 µm between the two diamonds in the cell. Then, the screws are tightened slightly to increase the pressure in the gasket. A couple of minutes are waited and then it is checked how much the thickness between the diamonds has decreased. This process is repeated until the thickness is reduced to about 50 µm. After this, a hole with a radius $r \leq culet\ length/3$ must be drilled in the centre of the area where the thickness has been reduced. An *Almax EasyLab Electrical Discharge Machining* (Fig. 10 right) with a drilling electrode of about 150 µm was used for this purpose.

To be able to characterize the measurements taken it is necessary to know at which pressure the sample is at any given time. To solve this problem, a small ruby ball is introduced into the hole where the sample and the pressure transmitting medium are, since the relationship between the luminescence and the pressure of the ruby is known. The pressure transmitting medium used is a mixture of ethanol-methanol-water with a 16:4:1 proportion.

Fig. 10. (Left) Diamond anvil cell with a gasket inside. (Centre) *Heidenhain ND221B length gauge*. (Right) *Almax EasyLab Electrical Discharge Machining*.

5. EXPERIMENTAL RESULTS AND DISCUSSION

5.1. Ambient conditions

5.1.1. Absorption

The absorption spectra have been measured with a spectrophotometer capable of taking absolute measurements and, in addition, the background of each of the spectra has been corrected. The results obtained corresponded to the combination of the absorption of the crystal plus the absorption of the Nd^{3+} ions, but the contribution of the crystal has been subtracted and the spectra obtained are presented in Figs. 11, 12 and 13.

As it can be noticed, the spectra are similar for the three garnet crystals in the sense that they show the same structure of bands. However, the magnitude of the absorption coefficient and transition probabilities, varies considerably with the sample, being larger for $LuAGG$ and smaller for $LuGG$. In fact, the results obtained for $LuAGG$ are about two times larger than those for $LuGG$. In the $LuAG$ sample the results are found between those of the other two samples, although they are closer to those of $LuGG$.

The electronic transitions induced by the absorption of radiation from the ${}^4I_{9/2}$ ground state to different excited states of the Nd^{3+} ion can be observed in the spectra. They have been identified through Dieke's diagram [42] and are indicated in the figures. As expected, each transition band has several peaks associated with it, showing the effect of the crystal-field interaction on the Nd^{3+} ions embedded in the garnets. These peaks are extremely sharp and indicate that Nd^{3+} ions occupy specific sites in the crystalline lattice, in this case, the positions of Lu^{3+} ions.

According to Smakula's equation, the larger the area under the band is, the higher the transition probability. The largest band in the three samples corresponds to the $^4I_{9/2} \rightarrow {}^4F_{5/2}, {}^2H_{9/2}$ transitions, located at around 808 nm. This wavelength will be used later to excite the samples for the luminescence and lifetime studies, since it is the wavelength at which they absorb the most. In addition, for $LuAGG$ there is another quite intense band associated with the $^4I_{9/2} \rightarrow {}^4F_{7/2}, {}^4S_{3/2}$ transition, at around 748 nm, and for $LuAG$ another one corresponding to the $^4I_{9/2} \rightarrow {}^4G_{7/2}, {}^2G_{5/2}$ transition, at around 589 nm.

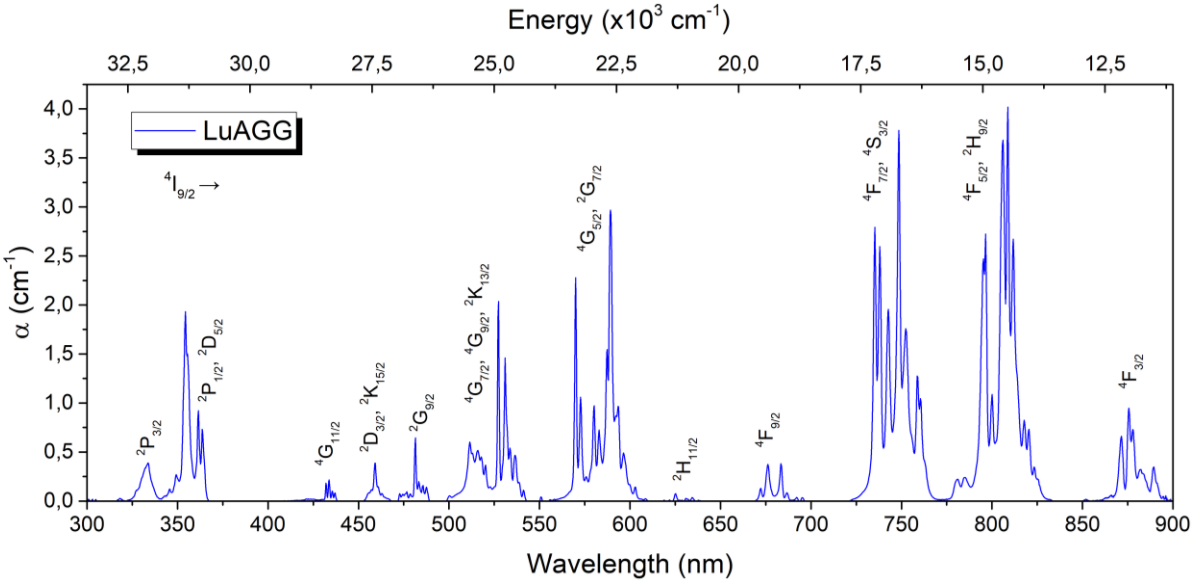

Fig. 11. Absorption spectrum of $LuAGG$ at ambient conditions. All transitions are from the $^4I_{9/2}$ ground state to the indicated multiplets.

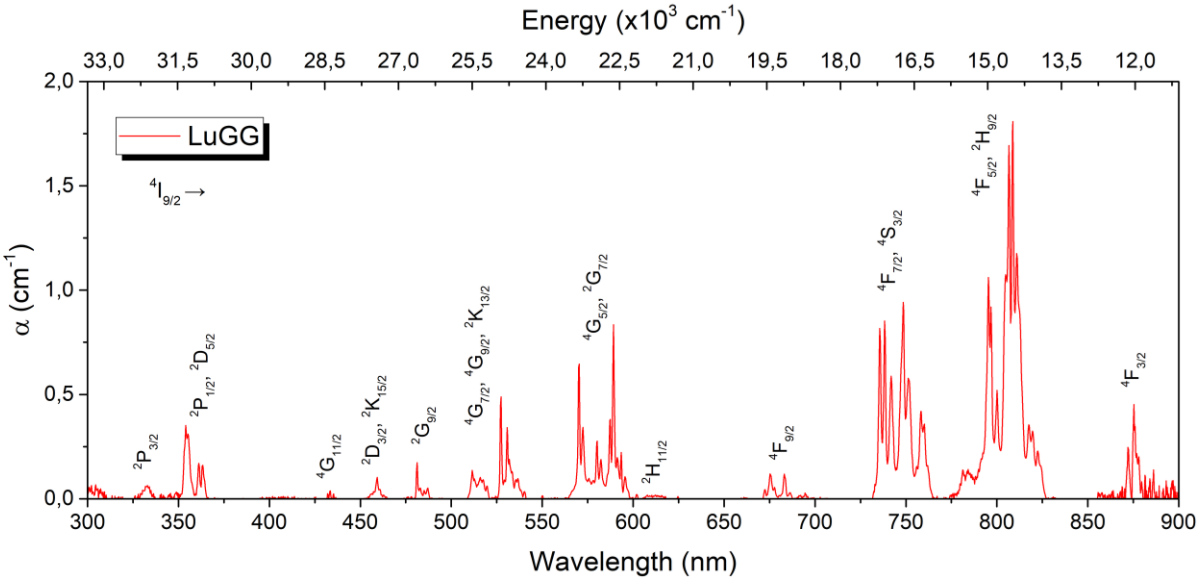

Fig. 12. Absorption spectrum of $LuGG$ at ambient conditions. All transitions are from the $^4I_{9/2}$ ground state to the indicated multiplets.

The spectra obtained have also been analysed according to the Judd-Ofelt theory. For this purpose, the doping ion concentration of the samples was determined and the refractive index

was taken from reference [43] and expressed in terms of the Sellmeier's formula. For $LuAGG$ it was not possible to find its refractive index and, therefore, it was taken an average value between $LuAG$ and $LuGG$ indexes. Results obtained are shown in Table 1. As one would expect, the transitions that have a highest oscillator strength are those to the excited states $^4F_{5/2}$, $^2H_{9/2}$, $^4F_{7/2}$, $^4S_{3/2}$ and $^2G_{5/2}$, $^4G_{7/2}$. These transitions are also the ones with the largest area in the three spectra. However, it should be noted that, in the case of $LuAGG$ nad $LuAG$, the transition to the $^2P_{1/2}$, $^2D_{5/2}$ states is the one with the highest oscillator strength, although in the spectrum it is not one of the transitions with the largest area. It has also been found that the oscillator strengths of the most intense transitions are considerably higher for $LuAGG$ than for the other two samples, even being between three to four times their value.

The experimental values obtained for the line strengths follow a similar pattern to those of the oscillator strengths, except in the case of the transition to the $^2P_{1/2}$, $^2D_{5/2}$ states, which is not the most intense for any of the samples. Furthermore, the calculated values show a great correspondence with the experimental ones, having the same order and, additionally, being very close to each other. The results obtained through the matrix elements from reference [19] and [44] do not differ much from each other, showing the same behaviour.

Apart from this, in Table 2, the calculated Judd-Ofelt parameters are presented, as well as the quality factor and the root mean square deviation. As it can be seen, negative values of the Ω_2 parameter were obtained, which makes no physical sense. This result can be explained by several factors, such as the determination of an average wavelength for the barycenter of the bands, the identification of the transitions and definition of their wavelength range, and the limitation on using bands up to 900 nm only. However, the main responsible reason is that only a few transitions depend on Ω_2, so its value is underestimated in the fitting. In addition, in the case of $LuAGG$ the refractive index used is not the real one, but merely an approximation, which can lead to substantial changes in the results obtained.

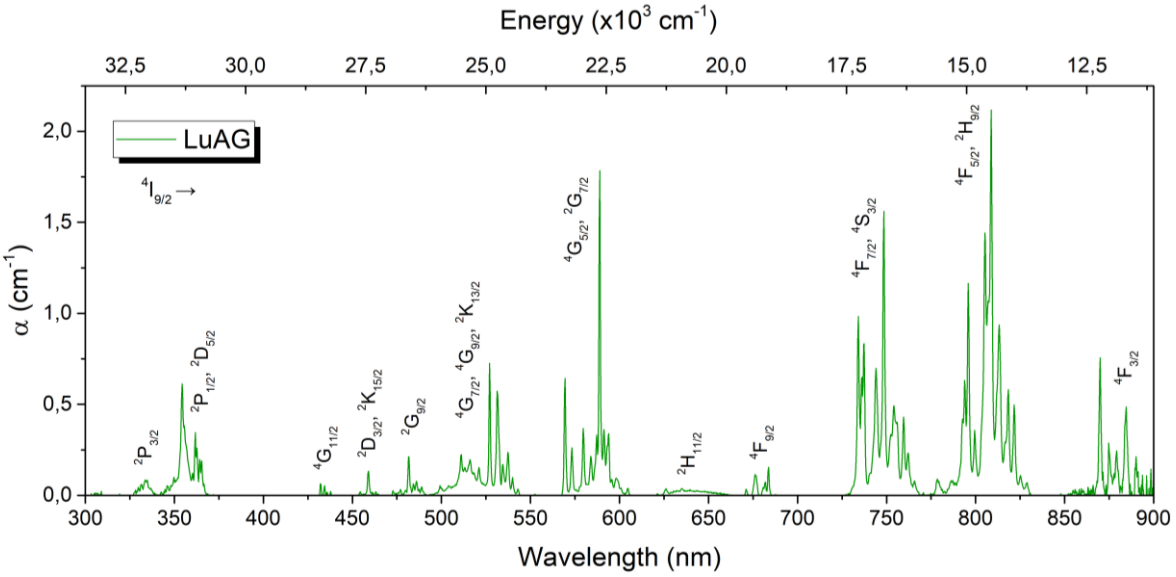

Fig. 13. Absorption spectrum of $LuAG$ at ambient conditions. All transitions are from the $^4I_{9/2}$ ground state to the indicated multiplets.

Table 1. Average wavelengths of the bands, oscillator strengths and experimental and calculated line strengths using the matrix elements from references [19] and [44].

		$^2P_{3/2}$	$^2P_{1/2}$, $^2D_{5/2}$	$^4G_{11/2}$	$^2D_{3/2}$, $^2K_{15/2}$	$^2G_{9/2}$	$^4G_{7/2}$, $^4G_{9/2}$, $^2K_{13/2}$	$^4G_{5/2}$, $^2G_{7/2}$	$^2H_{11/2}$	$^4F_{9/2}$	$^4F_{7/2}$, $^4S_{3/2}$	$^4F_{5/2}$, $^2H_{9/2}$	$^4F_{3/2}$
$\bar{\lambda}\ (nm)$	***LuAGG***	318	357	434	459	482	526	583	631	680	746	806	878
	LuGG	332	403	434	459	483	526	583	612	679	746	806	875
	LuAG	334	356	434	459	483	527	585	631	680	745	806	878
$f_{osc}\ (x\ 10^{-8})$	***LuAGG***	4	559	19	39	52	317	448	4	32	455	469	70
	LuGG	17	71	1	10	10	60	100	2	10	125	207	13
	LuAG	23	155	3	6	15	105	101	9	6	117	151	25
$S_{exp}\ (x\ 10^{-22}\ cm^2)$	***LuAGG***	1	98	4	9	13	85	134	1	11	177	197	32
	LuGG	3	14	0	2	2	16	30	1	4	49	89	6
	LuAG	4	27	1	1	4	28	30	3	2	45	62	11
$S_{cal}\ (x\ 10^{-22}\ cm^2)$ [19]	***LuAGG***	0	10	3	9	22	82	135	3	11	148	166	119
	LuGG	0	4	1	3	8	29	30	1	4	49	57	41
	LuAG	0	4	1	3	8	29	30	1	3	38	51	35
$S_{cal}\ (x\ 10^{-22}\ cm^2)$ [44]	***LuAGG***	1	8	3	9	7	78	135	3	13	184	186	62
	LuGG	0	3	1	3	2	26	30	1	5	64	65	22
	LuAG	0	3	1	3	2	25	30	1	4	49	56	23

Table 2. Calculated Judd-Ofelt parameters, quality factor X and root mean square deviation using the matrix elements from references [19] and [44].

	[19]			[44]		
	LuAG	***LuGG***	***LuAGG***	***LuAG***	***LuGG***	***LuAGG***
$\Omega_2\ (x\ 10^{-21}\ cm^2)$	-2	-2	-1	-3	-2	-1
$\Omega_4\ (x\ 10^{-21}\ cm^2)$	10	9	24	8	7	21
$\Omega_6\ (x\ 10^{-21}\ cm^2)$	5	7	21	7	9	26
$Quality\ factor\ X\ (a.u.)$	2.02	1.34	1.18	1.22	0.78	0.78
$\Delta rms\ (x\ 10^{-21})$	1	2	4	1	1	3

5.1.2. Luminescence

Luminescence measurements were carried out by exciting the garnets with a laser beam at a wavelength corresponding to the maximum peak of the absorption spectrum. In this way, the laser was tuned in 808 nm for the three samples, causing the excitation of the Nd^{3+} ions from the ground state $^4I_{9/2}$ to the excited states $^4F_{5/2}$ and $^2H_{9/2}$. Then, from these excited states, the Nd^{3+} ions decay by multiphonon de-excitation to the $^4F_{3/2}$ state, which is the multiplet from which the emission departs.

The three spectra, shown in Fig. 14, cover from 865 to 1455 nm, belonging to the near-infrared (NIR) interval of the electromagnetic spectrum. They were obtained with different set-ups and have been corrected from the instrument response. It is worth mentioning that the measurement range actually covered from 820 to 1700 nm, but in certain regions, there were no peaks distinguished. By means of the measured spectral range, it has been possible to study the transitions from the $^4F_{3/2}$ emitting level to the $^4I_{9/2}$ (ground state), $^4I_{11/2}$ and $^4I_{13/2}$ multiplets.

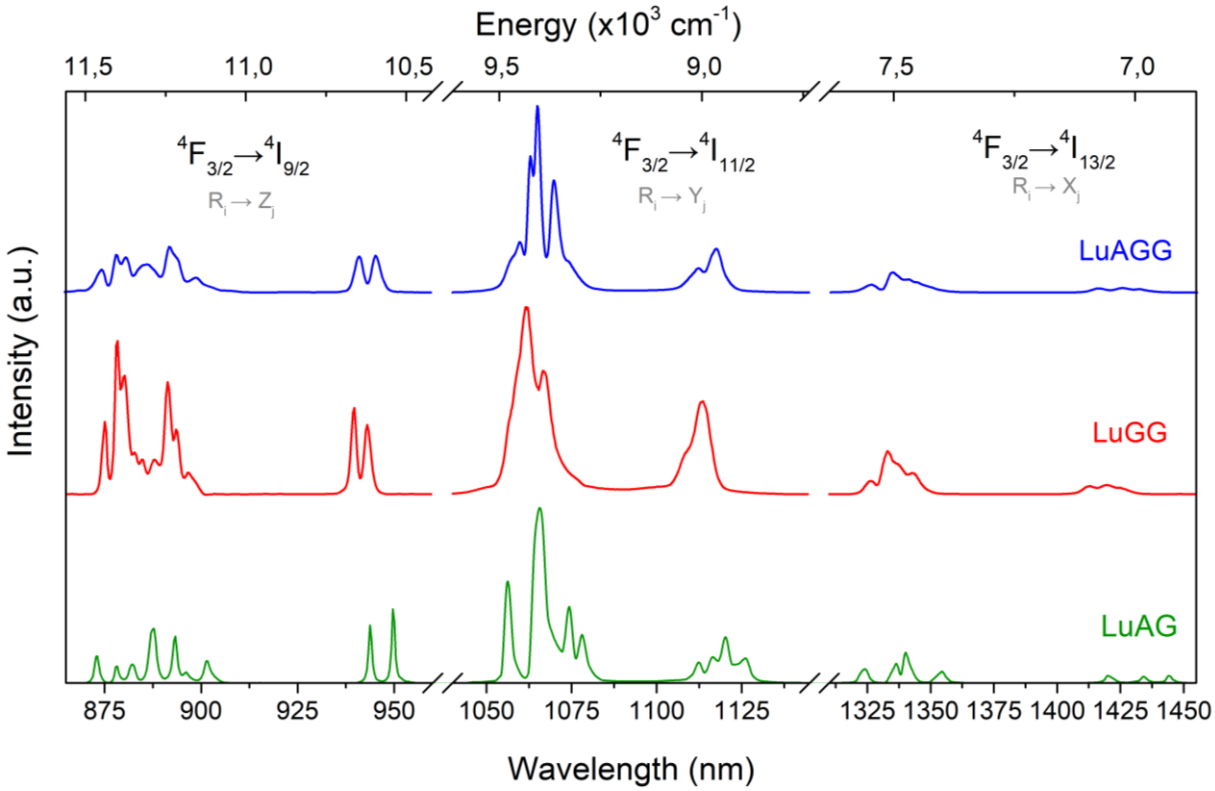

Fig. 14. Luminescence spectra of the the $LuAGG$, $LuGG$ and $LuAG$ samples at ambient conditions.

As it can be seen in Fig. 14, the structure of the bands corresponding to each of the transitions is not the same in all the samples, although theoretically the splitting of the levels should indeed be similar. These discrepancies can be explained on the basis that some peaks are strongly overlapped, as they are very close to each other. In addition, it can also be noticed that the $^4F_{3/2} \rightarrow {}^4I_{13/2}$ transition, which is the one in which more peaks should be observed (since

the ${}^4I_{13/2}$ multiplet splits into seven Stark levels when considering the crystal-field interaction), is actually the one in which less peaks are detected. Consequently, it can be concluded that the resolution of the set-up is not high enough to determine correctly the upper range of the NIR spectrum.

On the other hand, there are clear differences in the fine structure of bands of the three spectra. The $LuAGG$ and $LuGG$ ones are similar to each other, since several of their peaks are overlapped, making impossible to accurately identify some of the electronic transitions. In contrast, in the case of $LuAG$, the peaks are well separated and more clearly visible. Therefore, this sample is the one where most transitions can be seen. This phenomenon could be the result of a greater effect of the crystal-field interaction in the $LuAG$ garnet.

Moreover, as already explained, local symmetry at the Nd^{3+} sites in garnets is often described as an orthorhombic distortion of a main cubic symmetry [15] (see Fig. 2). Thus, two contributions must be considered when describing the crystal-field interaction: the cubic symmetry component and the superimposed non-cubic symmetry component. For the ${}^4F_{3/2}$ multiplet, it can be stated that the non-cubic contribution of the crystal-field interaction must be directly responsible for the observed splitting into the R_1 and R_2 Stark emitting levels. Following this, the energy gap between the $R_1 \rightarrow Z_5$ and $R_2 \rightarrow Z_5$ emissions transitions can be taken as a rough measurement of the magnitude of the crystal-field interaction.

When substituting the Ga ions for Al ions, the volume of the NdO_8 dodecahedron and the $Nd-O$ average distance (see Fig. 3) decrease and an increase of the splitting of the ${}^4F_{3/2}$ multiplet is expected. At ambient conditions, the larger the gap is, the larger the crystal-field strength affecting the Nd^{3+} ions and the orthorhombic distortion of the local environment are. On the contrary, a smaller energy gap suggests a lower crystal-field strength, associated with a local structure closer to the cubic one, which implies that the $Nd-O_1$ and $Nd-O_2$ distances tend to be equal. In Fig. 14, it can be seen that the $LuAG$ sample is the one with the largest energy gap between the transitions $R_1 \rightarrow Z_5$ and $R_2 \rightarrow Z_5$, while $LuGG$ is the one with the smallest one. Thus, it is confirmed that the intensity of the crystal-field interaction is higher in $LuAG$. The energy gap in $LuAGG$ is in an intermediate situation, although its more similar to the $LuGG$ one, so that it is possible to state that the crystalline structure of $LuAGG$ is closer to that of $LuGG$.

According to the Judd-Ofelt theory, the line strengths, spontaneous transition probabilities, branching ratios and radiative lifetimes of the three samples have been obtained and are shown in Table 3. The spontaneous transition probabilities reveal that the most probable transitions are those from the ${}^4F_{3/2}$ excited state to the ${}^4I_{9/2}$ (ground state) and ${}^4I_{11/2}$ ones. The results obtained considering the matrix elements given in references [19] and [44] are similar, although for $LuGG$ and $LuAG$, the most probable transition varies depending on the elements used. In contrast, for $LuAGG$ the most probable transition is, in both cases, the one in which the Nd^{3+} ions decay to the ${}^4I_{11/2}$ state. Regarding the radiative lifetimes obtained, there are remarkable differences between the $LuAGG$ sample and the other two ones, in which lifetimes

are almost three times larger. These differences may be caused by the unequal distribution of Nd^{3+} ions in the lattice of each sample.

Table 3. Average wavelength of the bands, line strengths, spontaneous transition probabilities, branching ratios and radiative lifetimes calculated using the matrix elements from references [19] and [44].

	$\boldsymbol{Transition}$	$\bar{\lambda}\ (\boldsymbol{nm})$	$\boldsymbol{S_{ED}}$ $(\boldsymbol{x\ 10^{-21}\ cm^2})$		$\boldsymbol{A_{ED}}\ (\boldsymbol{s^{-1}})$		$\boldsymbol{\beta}$		$\boldsymbol{\tau_{rad}}\ (\boldsymbol{\mu s})$	
	$^4F_{3/2} \rightarrow$		[19]	[44]	[19]	[44]	[19]	[44]	[19]	[44]
$\boldsymbol{LuAGG}$	$^4I_{9/2}$	899	7	6	1007	929	0.446	0.388	443	417
	$^4I_{11/2}$	1070	12	14	1053	1215	0.466	0.507		
	$^4I_{13/2}$	1356	4	6	187	239	0.083	0.100		
	$^4I_{15/2}$	1827	1	1	10	13	0.005	0.005		
$\boldsymbol{LuGG}$	$^4I_{9/2}$	896	2	2	358	313	0.470	0.392	1314	1254
	$^4I_{11/2}$	1073	4	5	341	400	0.448	0.502		
	$^4I_{13/2}$	1353	1	2	59	80	0.078	0.100		
	$^4I_{15/2}$	1824	0	0	3	4	0.004	0.005		
$\boldsymbol{LuAG}$	$^4I_{9/2}$	902	3	2	411	359	0.524	0.453	1276	1260
	$^4I_{11/2}$	1078	4	4	322	364	0.411	0.459		
	$^4I_{13/2}$	1355	1	1	49	66	0.062	0.083		
	$^4I_{15/2}$	1830	0	0	3	4	0.003	0.004		

The energy Stark levels for the $LuGG$ and $LuAG$ garnets had already been calculated in previous studies [45]. These values were represented in the spectra of Figs. 15 and 16 by small vertical lines, as a comparison to the experimental results. For $LuAG$, only the energy values of the transitions $^4F_{3/2} \rightarrow {}^4I_{9/2}$ and $^4F_{3/2} \rightarrow {}^4I_{11/2}$ were known from the reference. Furthermore, in the energy level diagrams of Fig. 17, the transitions that take place for the excitation of the ions as well as the de-excitation processes are shown for each of the samples.

The experimental results are very similar to the theoretical predicted values, coinciding in most cases. However, for $LuGG$, a certain shift is observed in the transitions $R_1 \rightarrow Z_5$ and $R_2 \rightarrow Z_5$. By means of the theoretical values and the Dieke's diagram [42], it has been possible to identify the transition corresponding to each of the spectrum peaks.

5.1.3. Lifetime

In order to measure the lifetime of the emitting level, each sample was excited with the OPO pulsed laser, tuned in about 808 nm, thus producing transitions from the $^4I_{9/2}$ ground state to the $^4F_{5/2}$ and $^2H_{9/2}$ excited states, which are very close in energy. After this, it was possible to display, in a digital oscilloscope, the temporal evolution of the luminescence of the Nd^{3+} ions from the $^4F_{3/2}$ excited state, to which they had previously decayed by multiphonon de-excitation from the $^4F_{5/2}$ and $^2H_{9/2}$ states, to the $^4I_{9/2}$ ground state.

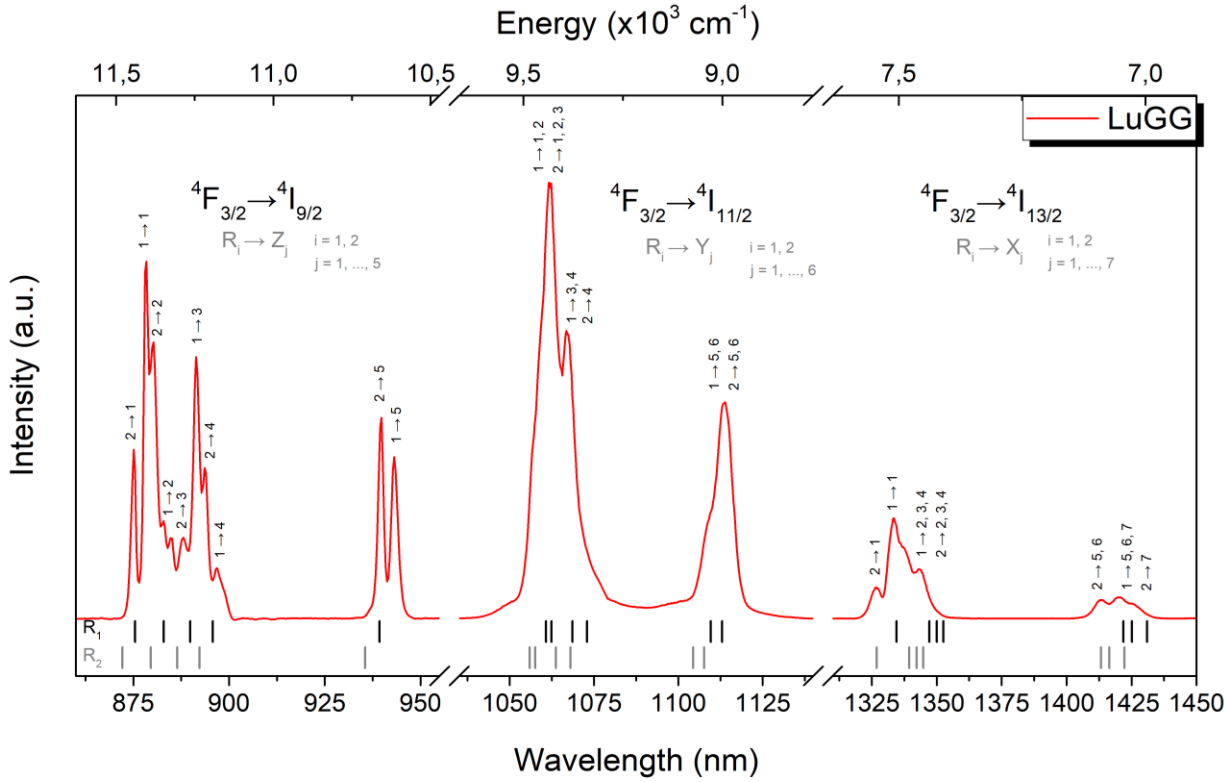

Fig. 15. Luminescence spectra of the $LuGG$ sample at ambient conditions. Energies of the emission peaks from reference [45] are shown as vertical lines at the bottom of the representation.

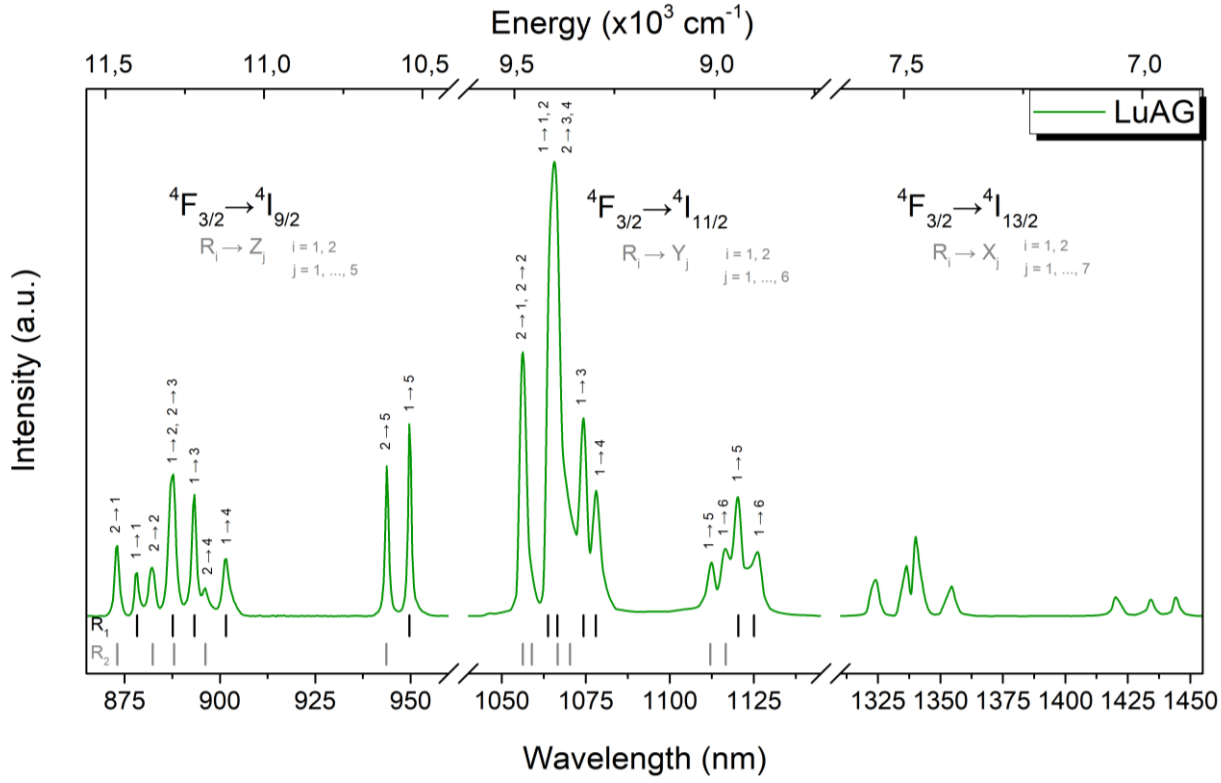

Fig. 16. Luminescence spectra of the $LuAG$ sample at ambient conditions. Energies of the emission peaks from reference [45] are shown as vertical lines at the bottom of the representation.

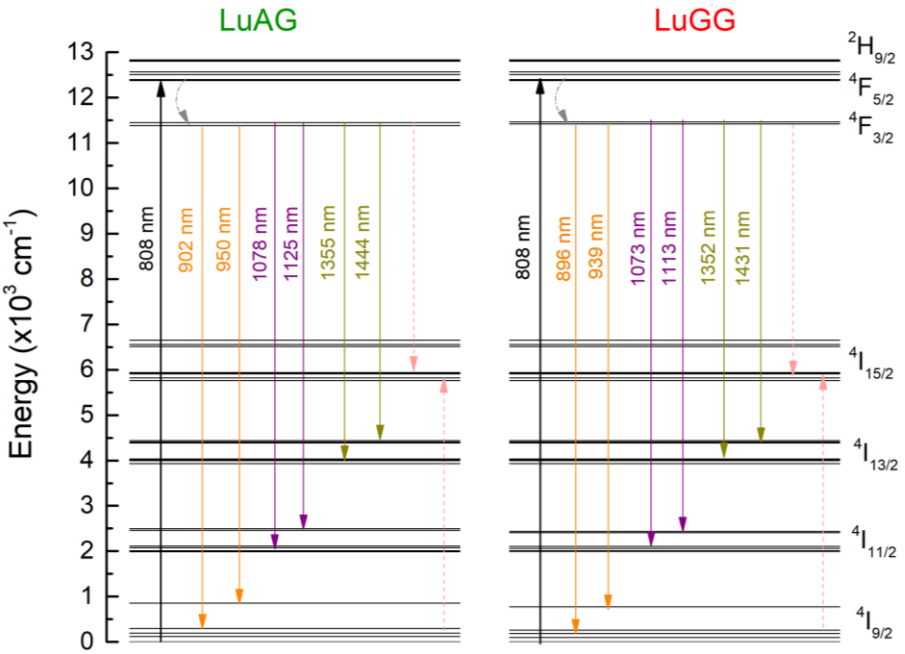

Fig. 17. Partial energy levels diagrams of the Nd^{3+}ions embedded in the $LuGG$ (left) and $LuAG$ (right) lattices. Excitation and de-excitation processes are represented using arrows labelled with their corresponding energies. In addition, multiphonon de-excitation and cross-relaxation processes are shown in dashed lines.

The luminescence decay curve of each of the garnets is shown in logarithm scale in Fig. 18. At first, the curve might seem to be exponential, however, when trying to adjust it to a single exponential one, it turns out not to be possible. The non-exponential nature of the curves indicates that the de-excitation of the Nd^{3+} ions is not purely radiative and due to the creation of phonons, but that there are also energy transfer processes between Nd^{3+} ions involved. These processes become more important as the concentration of optically active ions in the sample increases, reducing the distances between them and, consequently, increasing the multipolar interactions between them. In addition, the formation of $Nd^{3+} - Nd^{3+}$ pairs and the small fraction of Nd^{3+} ions that are positioned in octahedral sites may also contribute to the non-exponential behaviour of the decay curves [46].

The experimental values of the lifetimes were obtained by means of Eq. (28) and are shown in Table 4. It is observed that the $LuAG$ sample has the shortest lifetime, 208 μs, and the $LuGG$ one has the longest one, 229 μs. As it would be expected, the lifetime of $LuAGG$, which contains both aluminium and gallium atoms, is between these two values, 220 μs. The difference on these values shows the influence of the characteristic structure of the lattice in which the Nd^{3+} ions are embedded when they are de-excitated. Moreover, as it can be noticed, the experimental lifetimes differ greatly from the radiative ones calculated through the Judd-Ofelt theory, which are also shown in Table 4. This difference has to be ascribed to the existence of non-radiative processes, multiphonon de-excitation and energy transfer processes, which are highly significant in the samples studied, especially in the case of $LuGG$ and $LuAG$, where the radiative lifetimes are almost six times higher than the experimental ones.

Due to the non-exponential behaviour of the decay curves, it was decided to fit the experimental data to the Inokuti-Hirayama model, following Eq. (29). The parameters τ_0 and Q were treated as free parameters and the fitting was tested for the different values of S ($S = 6, 8, 10$), to determine which interaction mechanism was the predominant one, depending on how well it could reproduce the acquired data. It was observed that for the three samples, the best fitting was achieved considering $S = 6$, so it was concluded that the dipole-dipole interactions between Nd^{3+} ions are the predominant ones in the lutetium garnets. From the fitting curves, the values of the donor lifetime in the absence of the acceptor, or intrinsic lifetime, τ_0 were obtained, as well as those of the dimensionless parameter Q.

The results obtained follow the same pattern as the experimental values: $LuAG$ has the shortest lifetime, $LuGG$ the longest one and $LuAGG$ value is in the middle between these two. However, it is observed that the lifetimes obtained through the model are slightly higher than the experimental ones. Specifically, the difference between the results is around 8 and 8.7 %.

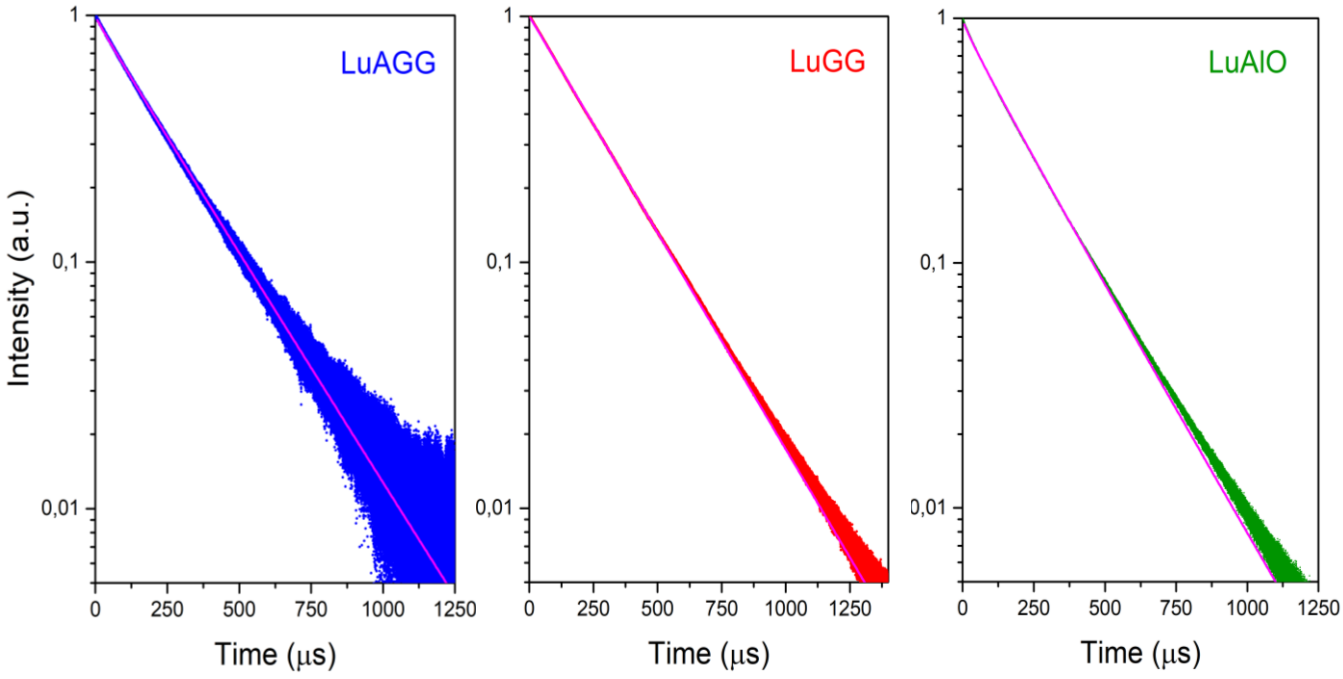

Fig. 18. Luminescence decay curve for the ${}^4F_{3/2} \rightarrow {}^4I_{9/2}$ transition for $LuAGG$ (left), $LuGG$ (middle) and $LuAG$ (right) at ambient conditions, including the Inokuti-Hirayama fitted curves considering $S = 6$.

Table 4. Experimental lifetimes of the three garnets for the ${}^4F_{3/2} \rightarrow {}^4I_{9/2}$ transition, as well as radiative lifetimes obtained as an average of the ones calculated using the matrix elements of references [19] and [44] and characteristic parameters, τ_0 and Q, of the fitting to the Inokuti-Hirayama model.

	τ_{exp} (μs)	τ_{rad} (μs)	τ_0 (μs)	Q
LuAGG	220	430	239.41 ± 0.01	0.08942 ± 0.00006
LuGG	229	1284	246.795 ± 0.004	0.00258 ± 0.00006
LuAG	208	1268	225.86 ± 0.01	0.19518 ± 0.00004

5.1.4 Upconversion

The experiment that was conducted to determine if any sample show upconversion processes consisted in a laser that could excite the samples and whose emission was tuned in a wavelength at which they showed a maximum absorption, specifically at 808.7 nm. If there is upconversion, once the laser beam reaches the sample, visible light should be observed inside the sample as a consequence. However, this phenomenon was not observed in any of the three samples. Therefore, it was concluded that none of the samples show upconversion processes.

5.2. Extreme conditions

5.2.1. Low temperature measurements

A study of the luminescence of the $LuAG$ and $LuAGG$ samples with temperature was carried out in order to calibrate these materials as temperature sensors. In this sense, the samples were excited with a laser tuned in 808 nm, inducing transitions from the ${}^4I_{9/2}$ ground state to the ${}^4F_{5/2}$ and ${}^2H_{9/2}$ excited states. As already mentioned in the luminescence measurements at ambient conditions, the Nd^{3+} ions decay by multiphonon de-excitation from these last two levels to the ${}^4F_{3/2}$ emitting level and from this one to the ground state ${}^4I_{9/2}$ again.

Before starting to study the effect of temperature on the sample, it was necessary to check experimentally whether the working power of the laser could cause the sample to heat up. For this purpose, at room temperature, a *TPM-300 Laser Power Meter* was added to the set-up right at the cryostat input. Then, measurements of the sample emission spectra were taken modifying the laser power. Once this was done, the method used to check whether the laser power had any thermal effect on the sample was to correct the background of each of the spectra and normalize them so that they could be compared with each other in the same representation. After studying the relative intensities of the normalized spectra, it was concluded that the laser power was not related to a heating of the sample that could be significantly appreciated and, therefore, this effect was neglected. Finally, the working power used was of 50 mW.

The measured spectra covered the range from 865 to 955 nm, registering the ${}^4F_{3/2} \rightarrow {}^4I_{9/2}$ $(R_i \rightarrow Z_j)$ transition. They were measured from the minimum temperature that was reached with the vacuum pump used (58 K in the case of $LuAGG$ and 40 K for $LuAG$) up to room temperature, at intervals of about 30 K. The spectra, shown in Figs. 19 and 20, have been corrected from the instrument response.

Firstly, given the transition studied, it should be possible to observe a total of ten peaks. At low temperature it is possible to distinguish these ten peaks in both samples, however, when temperature rises, an overlapping phenomenon is noticed in some of the peaks, causing some of them to be indistinguishable.

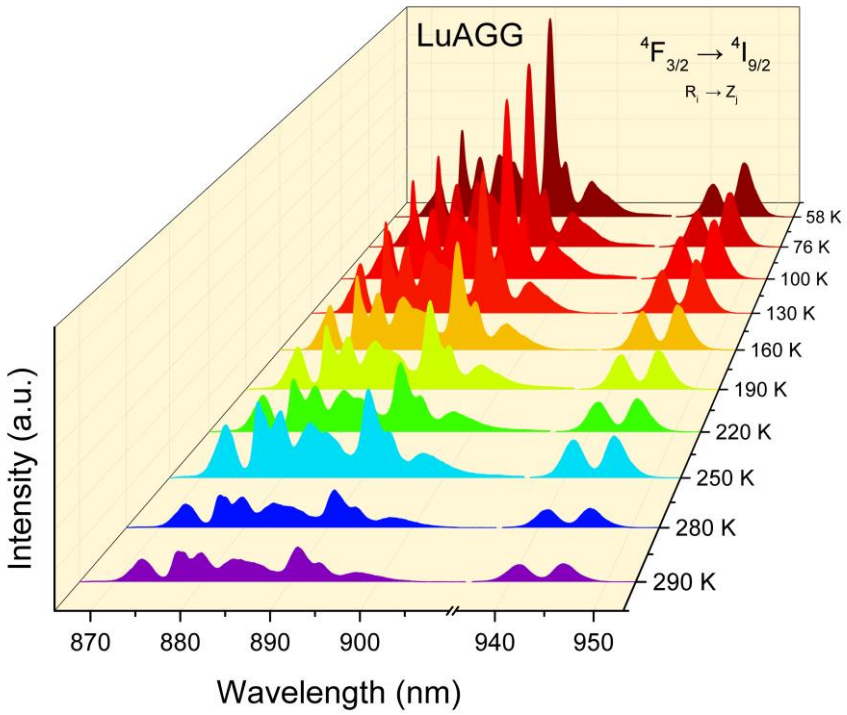

Fig. 19. Luminescence spectra of the $LuAGG$ sample under low temperature conditions showing the $^4F_{3/2} \rightarrow {}^4I_{9/2}$ transition.

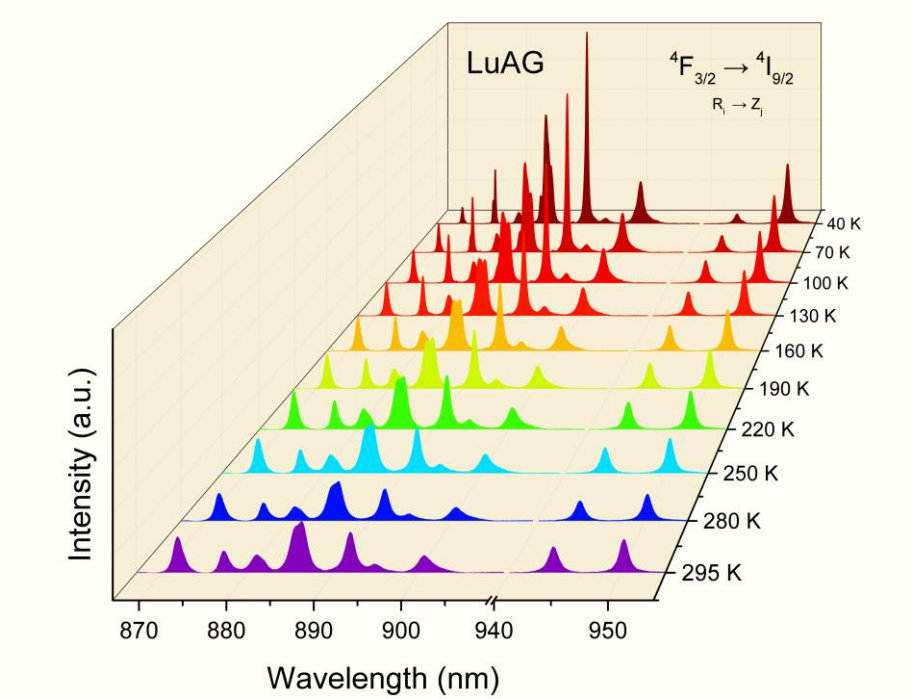

Fig. 20. Luminescence spectra of the $LuAG$ sample under low temperature conditions showing the $^4F_{3/2} \rightarrow {}^4I_{9/2}$ transition.

In addition, a substantial difference can be observed when comparing the spectrum obtained for each of the samples. For $LuAG$, the peaks show a very slight overlap and are quite far apart from each other, so it is very easy to distinguish them. Whereas, in the case of the $LuAGG$ sample, the peaks show a considerably greater overlapping, causing the formation of two bands. This result supports the spectra measured under ambient conditions, where the hypothesis that there was a greater effect of the crystal-field interaction on the $LuAG$ crystal was already advanced, causing the peaks to be better distinguished.

Furthermore, in order to use these samples as temperature sensors, the Luminescence Intensity Ratio (LIR) technique was applied. The study that was carried out was focused on the transitions $R_1 \rightarrow Z_5$ and $R_2 \rightarrow Z_5$ and consisted on determining the relative intensity of each one of the peaks corresponding to these transitions through integration. These results were introduced into Eq. (31) to establish a calibration for each of the samples. The fitting equation used was Eq. (37) and the results of the fitting can be consulted in Fig. 21.

$$ln\,(LIR)\; = \; -C/T \; + \; ln\,(A) \qquad (37)$$

where the parameter C represents $C = \Delta E/k_B$, taking the value for the Boltzmann's constant as $k_B = 1.3806\,J/K \approx 0.695\,cm^{-1}/K$ and A is the constant introduced in Eq. (31). In addition, through this fitting, the energy difference between transitions was calculated to compare it with the values from reference [45]. For $LuAG$, an energy gap of 50 ± 2 cm^{-1} was obtained, being the value of the reference 67 cm^{-1}, whereas for the $LuAGG$ the result obtained was 28 ± 2 cm^{-1}, being the value of the reference 43 cm^{-1}. In both cases, the values obtained are of the same order, although the reference values are not within the margin of experimental error. These results, as well as the value of the constant $\ln(A)$ of the Eq. (37) are presented in Table 5.

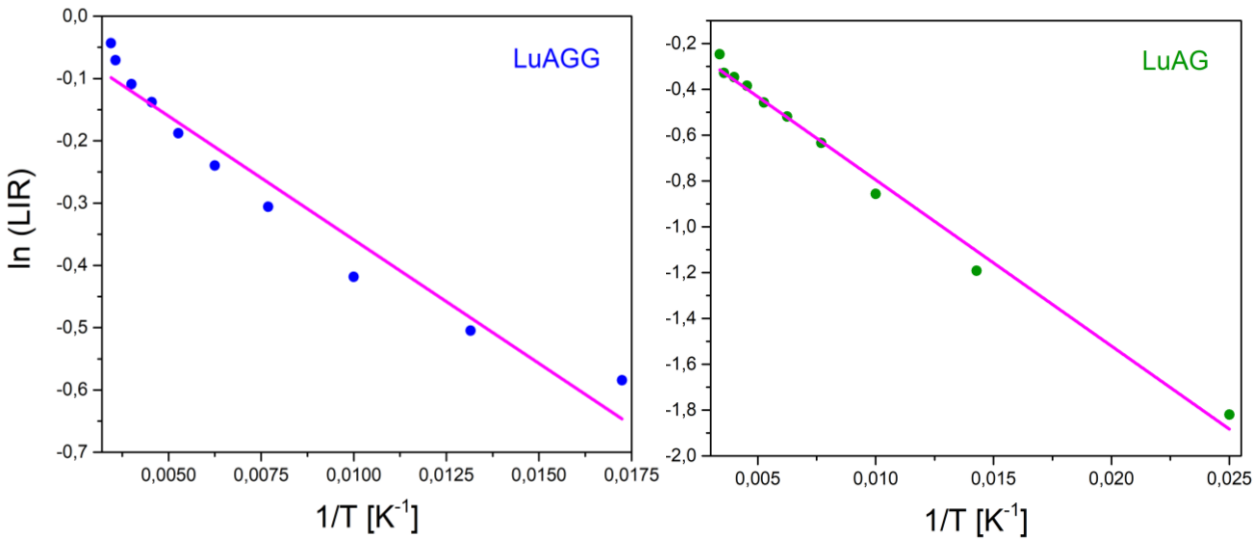

Fig. 21. Fitting of the experimental results to Eq. (37) calculated for the LIR study for $LuAGG$ and $LuAG$.

Table 5. Energy gaps between the $R_1 \rightarrow Z_5$ and $R_2 \rightarrow Z_5$ transitions calculated through the LIR method and values obtained from reference [45]. The dimensionless constant $\ln(A)$ has also been added.

	$\Delta E_{exp}\ (cm^{-1})$	$\Delta E_{ref}\ (cm^{-1})$	$ln(A)$
LuAGG	28 ± 2	43	1.04 ± 0.03
LuAG	50 ± 2	67	0.93 ± 0.02

Finally, as common when characterizing temperature sensors, the relative sensitivity, calculated from Eq. (32), has been plotted in Fig. 22. It has been decided to represent both the values obtained by considering the experimental and reference energy gaps for comparison purposes. As it can be seen, the relative sensitivity of the $LuAG$ is about 4 times higher than that of the $LuAGG$, which is an indicator that the quality of the $LuAG$ as a temperature sensor is better than that of the $LuAGG$.

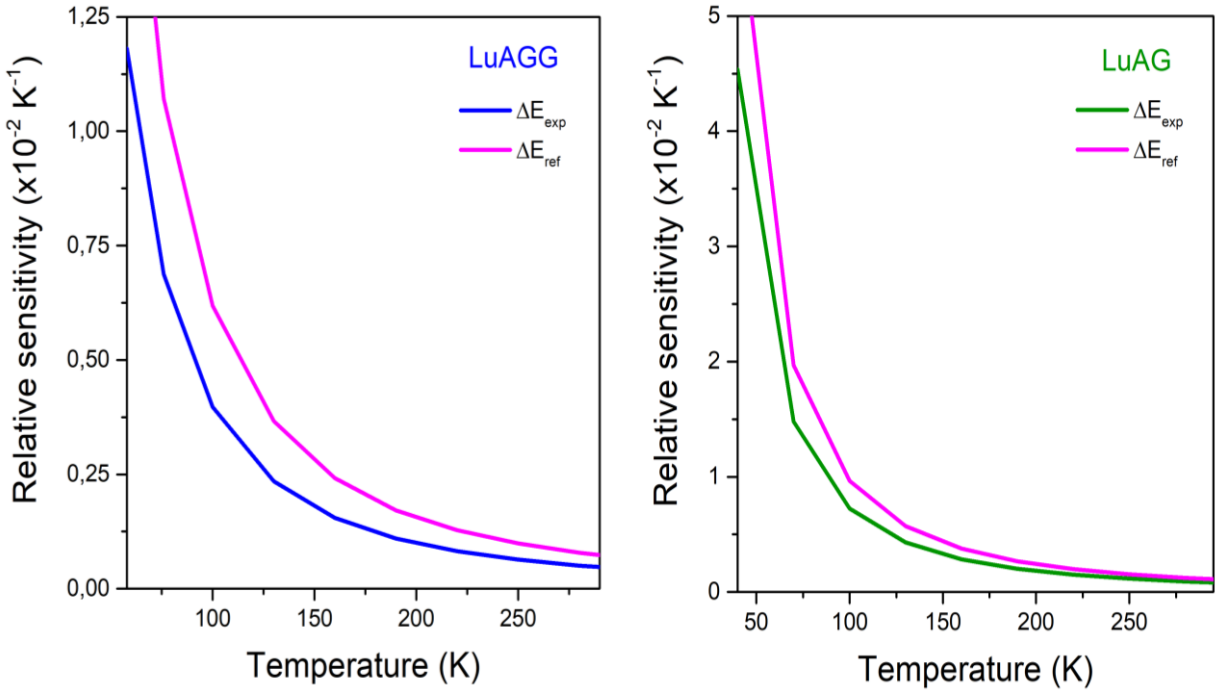

Fig. 22. Relative sensitive of the $LuAGG$ and $LuAG$ samples using the energy gap calculated through the fitting and the one taken from reference [45].

5.2.2. High pressures measurements

In order to determine the pressure of the samples contained on the DAC, a new system based on that suggested by K. Syassen [32], shown in Fig. 23, was developed. The material used to build the instrument was purchased from the US company *Newport*, specialized in the development and manufacture of technological products for scientific research.

This material consisted mainly of several mechanical components (stainless steel metal rods, optical cages, optical rail carriers, two bearing metric linear stages, two micrometric screws and holders for lenses and optical filters), as well as a beam splitter cube, a broadband dielectric or dichroic beam splitter and a 20x objective.

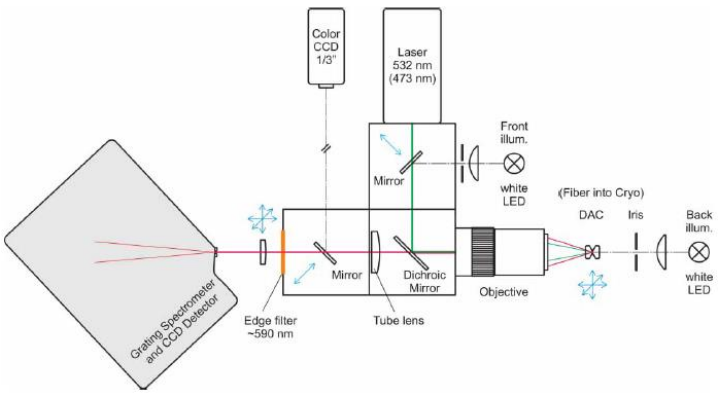

Fig. 23. Scheme of the portable ruby luminescence system for pressure measurement.

Once the material was received, it started the assembly of the device on an optical table. Firstly, the mechanical elements were set up: the optical cages were connected through metal rods and placed over supports that were fixed to the optical table. Then, the system where the DAC would be placed was prepared. Since the laser beam had to focus on the sample, it was necessary for the system used to be able to move in the three space directions, in order to carry out a proper centring. Therefore, a base with three sliding bearing metric linear stages (one for each axis of movement) with micrometric screws was designed to accurately adjust the position of the sample. After this, the 20x objective and a 405 nm low-power laser to excite the sample were placed in their respective positions. It was necessary to build some plastic components using a 3D printer in order them with the system. Finally, the optical elements needed for the proper functioning of the device (a converging 10 cm focal length lens, the broadband dielectric beamsplitter and a detector) were placed (see Fig. 24).

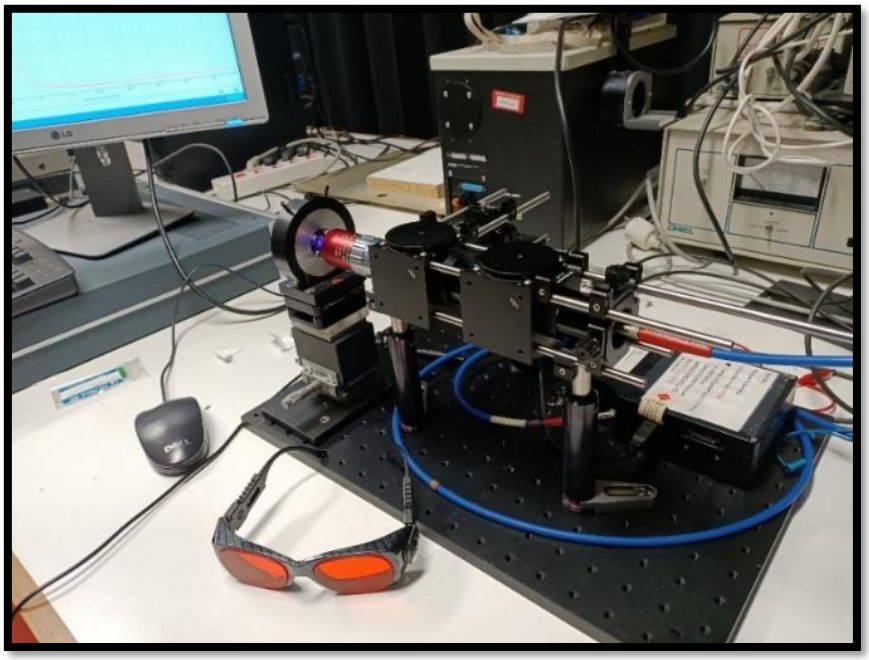

Fig. 24. Ruby luminescence measuring instrument.

The operation of the device is based on the following procedure. Firstly, the laser strikes the dichroic beam splitter, which is at 45º and is able to send the light towards the DAC. The light beam passes through the microscopic objective and reaches the sample, exciting it. Then, the sample produces an emission that is collected by the objective. This light goes through the dichroic beam splitter in the opposite direction than the previous one and gets to a converging lens that focuses the beam on a detector (optical fibre). This radiation is analysed through a *Spectra Suite spectrometer* connected to a *CCD Ocean Optics camera*. By monitoring the emission of the ruby in a computer software, it is possible to precisely calibrate the position of the DAC, by manipulating the micrometric screws of the base on which it is placed.

As it can be noticed, the system built is highly handy and simple to use. To determine the pressure of the sample in the DAC, it is only necessary to place it on its base on the instrument, turn on the laser and measure the emission spectrum using the computer software. Once this has been done, the pressure of the sample can be determined by calculating the shift of the emission bands. As a result, the time required to take a measurement is less than 5 minutes. In addition, the device has been prepared for possible improvements to implement its operating features.

The instrument was tested placing a DAC which contained several ruby balls to check that its characteristic R_1 and R_2 emission lines could be seen. Unfortunately, it was impossible to take high pressure luminescence measurements, given the sanitary emergency issue that forced the lockdown of the *University of La Laguna*.

6. CONCLUSIONS

Optical spectroscopy measurements carried out on the three lutetium garnets, both at ambient conditions and at low temperature conditions, have allowed to perform a characterization of them.

Regarding ambient measurements, it has been possible to determine the most probable transitions through which the samples are able to absorb radiation of different wavelengths by comparing the oscillator strengths and the line strengths obtained by means of the Judd-Ofelt theory. These values were later used to efficiently excite the samples for the emission spectra and the decay curves of the lifetimes. In this sense, it has been possible to identify some of the characteristic de-excitation transitions ($^4F_{3/2} \rightarrow {}^4I_{9/2}$, $^4I_{11/2}$, $^4I_{13/2}$), corresponding to the NIR range of the electromagnetic spectrum, and to calculate their spontaneous transition probabilities, as well as their line strengths and branching ratios. Through the spectra obtained it has also been possible to observe the effect of the crystal-field interaction in each of the samples, proving that in $LuAG$ it is significantly larger than in the other two samples, which showed overlapping phenomena.

The calculated lifetimes corresponding to the $^4F_{3/2} \rightarrow {}^4I_{9/2}$ transition are of the same order. Specifically, the lifetime for $LuGG$ is the highest of the three ones and the one for $LuAG$

the lowest, having $LuAGG$ an intermediate value between those two, as it is composed of both elements (gallium and aluminium). Furthermore, the results of the fitting to the Inokuti-Hirayama model show that the predominant interaction between the Nd^{3+} ions embedded in the lattice corresponds to the electric dipole-dipole kind. Likewise, the values derived for the intrinsic lifetime of the donor in the absence of the acceptor τ_0 are similar to the experimental ones, and also show that $LuGG$ has the highest value while $LuAG$ has the lowest one. On the contrary, the calculated radiative lifetimes present a large discrepancy in relation to the experimental values, which may be a consequence of the fact that non-radiative processes are quite important in the samples studied.

On the other hand, it was also proven that none of the samples show upconversion emission, as no signal was observed when the samples were irradiated with an IR laser beam.

Finally, by studying the relationship of luminescence with temperature, it was possible to examine the effect of low temperatures on the transitions between the split levels corresponding to the ${}^4F_{3/2} \rightarrow {}^4I_{9/2}$ transition. It was observed that, while in $LuAG$ the peaks were well separated and distinguished from each other, in $LuAGG$ some peaks overlapped, making it difficult to identify them. In this sense, the phenomenon already observed in the emission spectra under ambient conditions was confirmed, indicating that the effect of the crystal-field interaction is notably greater in $LuAG$ than in the other samples. Besides, by means of the LIR study of the transitions $R_1 \rightarrow Z_5$ and $R_2 \rightarrow Z_5$, it was possible to obtain the energy gap between these transitions, as well as to establish a calibration that allows the use of the samples as temperature sensors.

7. RESUMEN EN ESPAÑOL

Este trabajo tiene como objetivo analizar las propiedades ópticas de tres cristales granates dopados al 1 wt% con iones Nd^{3+}. Dichos granates tienen la siguiente composición química $Nd{:}Lu_3Ga_3Al_2O_{12}$, $Nd{:}Lu_3Al_5O_{12}$ y $Nd{:}Lu_3Ga_5O_{12}$, aunque para facilitar la referencia se utilizarán los nombres $LuGAG$, $LuAG$ y $LuGG$, respectivamente.

En la introducción se explican conceptos generales como, por ejemplo, en qué consiste la espectroscopía y cómo se puede usar para estudiar propiedades ópticas de los materiales. Asimismo, se mencionan los granates que se van a estudiar y la relevancia del uso de los mismos en el diseño de láseres de estado sólido. Por otra parte, también se destaca la necesidad del estudio de las propiedades ópticas bajo condiciones extremas de presión y temperatura para poder entender lo que ocurre en sistemas físicos en los que se den estas condiciones.

En la siguiente sección se plantean los objetivos del trabajo y se explica cómo se va a proceder para poder obtener información sobre las muestras a través de los espectros medidos.

A continuación, se desarrollan los conceptos teóricos necesarios para poder ser capaces de entender y analizar los resultados obtenidos. Se comienza explicando las propiedades y estructura electrónica de los lantánidos, pues los granates utilizados están dopados con iones trivalentes del neodimio Nd^{3+}. Seguidamente, para poder caracterizar los niveles de energía de los compuestos utilizados se exponen los términos que forman el hamiltoniano del sistema, teniendo en cuenta las interacciones que sufre la molécula debido a la presencia de iones dopantes en su entorno y, además, se explica detalladamente cómo es la estructura cristalográfica de las muestras. Por otra parte, se desarrollan conceptos espectroscópicos como la ley de Lambert-Beer y la fuerza de oscilador, así como su relación con la teoría de Judd-Ofelt. Tras esto, se presentan los diferentes métodos por los que un sistema puede decaer desde un estado excitado al estado fundamental y se relacionan con el tiempo de vida, el cual se puede calcular también a través del ajuste al modelo de Inokuti-Hirayama. A continuación, se explica en qué consiste la técnica LIR (relación entre las intensidades de la luminiscencia) y se facilita una expresión para el cálculo de la sensibilidad relativa. Finalmente, se destacan algunas de las propiedades del rubí y se detalla su amplio uso como sensor de presión en celdas de yunque de diamante.

En la quinta sección se presenta cómo fue el desarrollo experimental. Más concretamente, se explica cómo se crecieron las muestras, los equipos experimentales que se utilizaron para la toma de medidas y las condiciones en las que se tomó cada una de ellas.

El apartado de análisis de resultados se ha dividido en dos secciones: condiciones ambiente y bajas temperaturas. En cuanto a los resultados de condiciones ambiente, se adjuntan los espectros de absorción y emisión obtenidos para cada una de las tres muestras, los cuales se analizan detalladamente para explicar las características que diferencian a unas muestras de otras. Con este mismo fin, se han obtenido los parámetros de Judd-Ofelt, que permiten explicar de forma cuantitativa los resultados de los espectros. Además, en relación a los espectros de emisión, también se ha añadido una comparación entre las energías de las transiciones correspondientes a los resultados experimentales con resultados de la bibliografía. En esta sección también se presentan las curvas de decaimiento de los iones Nd^{3+} en cada muestra, con las que se han podido calcular los tiempos de vida característicos del estado excitado $^4F_{3/2}$. Estos tiempos se han comparado tanto con los tiempos de vida radiativos, obtenidos mediante la teoría de Judd-Ofelt, como con los tiempos de vida intrínsecos obtenidos a partir del ajuste al modelo de Inokuti-Hirayama. Por otra parte, en la sección de bajas temperaturas, se muestran los resultados obtenidos de la luminiscencia de las muestras al variar la temperatura. Asimismo, se realiza un estudio LIR para cada muestra, con el fin de poder calibrarlas para ser usadas como sensores de temperatura.

Tras esto, se exponen las conclusiones en las que se detallan y explican los resultados más relevantes obtenidos en la sección previa.

REFERENCES

[1] Cavaliere, S., Foccoli, P., & Farina, P. L. (1988). Nd: YAG laser bronchoscopy: a five-year experience with 1,396 applications in 1,000 patients. *Chest*, *94*(1), 15-21.

[2] Romanos, G. E. (1994). Clinical applications of the Nd: YAG laser in oral soft tissue surgery and periodontology. *Journal of clinical laser medicine & surgery*, *12*(2), 103-108.

[3] Bachmann, F. G. (1990). Industrial laser applications. *Applied Surface Science*, *46*(1-4), 254-263.

[4] Holzapfel, W. B., & Isaacs, N. S. (1997). *High pressure techniques in chemistry and physics-a practical approach* (p. 398).

[5] Sinha, S. P. (2013). *Complexes of the rare earths*. Elsevier.

[6] Liu, G., & Jacquier, B. (Eds.). (2006). *Spectroscopic properties of rare earths in optical materials* (Vol. 83). Springer Science & Business Media.

[7] Condon, E. U., & Odabasi, H. (1980). *Atomic structure*. CUP Archive.

[8] Bethe, H. (1929). Termaufspaltung in kristallen. *Annalen der Physik*, *395*(2), 133-208.

[9] Van Vleck, J. H. (1932). Theory of the variations in paramagnetic anisotropy among different salts of the iron group. *Physical Review*, *41*(2), 208.

[10] Burns, R. G. (1993). *Mineralogical applications of crystal field theory* (Vol. 5). Cambridge university press.

[11] García-Solé, J., Bausa, L., & Jaque, D. (2005). *An introduction to the optical spectroscopy of inorganic solids*. John Wiley & Sons.

[12] Hahn, T., Shmueli, U., & Arthur, J. W. (Eds.). (1983). International tables for crystallography (Vol. 1, pp. pp-182). Dordrecht: Reidel.

[13] Monteseguro, V., Rodríguez-Hernández, P., Ortiz, H. M., Venkatramu, V., Manjón, F. J., Jayasankar, C. K., ... & Muñoz, A. (2015). Structural, elastic and vibrational properties of nanocrystalline lutetium gallium garnet under high pressure. *Physical Chemistry Chemical Physics*, *17*(14), 9454-9464.

[14] León-Luis, S. F., Muñoz-Santiuste, J. E., Lavín, V., & Rodríguez-Mendoza, U. R. (2012). Optical pressure and temperature sensor based on the luminescence properties of Nd 3+ ion in a gadolinium scandium gallium garnet crystal. *Optics express*, *20*(9), 10393-10398.

[15] Rodríguez-Mendoza, U. R., León-Luís, S. F., Muñoz-Santiuste, J. E., Jaque, D., & Lavín, V. (2013). Nd^{3+}-doped $Ca_3Ga_2Ge_3O_{12}$ garnet: A new optical pressure sensor. *Journal of Applied Physics*, *113*(21), 213517.

[16] Görller-Walrand, C., & Binnemans, K. (1996). Rationalization of crystal-field parametrization. *Handbook on the physics and chemistry of rare earths*, *23*, 121-283.

[17] San Fabian, E. (2019). *Química Cuántica y Espectroscopía*. Universidad de Alicante, sección de Química Física.

[18] Smakula, A. (1930). Über erregung und entfärbung lichtelektrisch leitender alkalihalogenide. *Zeitschrift für Physik*, *59*(9-10), 603-614.

[19] Carnall, W. T., Crosswhite, H., & Crosswhite, H. M. (1978). Energy level structure and transition probabilities in the spectra of the trivalent lanthanides in LaF_3 (No. ANL-78-XX-95). Argonne National Lab.(ANL), Argonne, IL (United States).

[20] Judd, B. R. (1962). Optical absorption intensities of rare-earth ions. *Physical review*, *127*(3), 750.

[21] Ofelt, G. S. (1962). Intensities of crystal spectra of rare-earth ions. *The journal of chemical physics*, *37*(3), 511-520.

[22] Méndez-Ramos, J., Lavın, V., Martın, I. R., Rodrıguez-Mendoza, U. R., González-Almeida, J. A., Rodrıguez, V. D., ... & Núñez, P. (2001). Optical properties of Er3+ ions in transparent glass ceramics. *Journal of alloys and compounds*, *323*, 753-758.

[23] Choi, J. H., Margaryan, A., Margaryan, A., & Shi, F. G. (2005). Judd–Ofelt analysis of spectroscopic properties of Nd3+-doped novel fluorophosphate glass. *Journal of luminescence*, *114*(3-4), 167-177.

[24] Weber, M. J. (1968). Radiative and multiphonon relaxation of rare-earth ions in Y 2 O 3. *Physical Review*, *171*(2), 283.

[25] Venkatramu, V., León-Luis, S. F., Rodríguez-Mendoza, U. R., Monteseguro, V., Manjón, F. J., Lozano-Gorrín, A. D., ... & Lavín, V. (2012). Synthesis, structure and luminescence of Er 3+-doped Y 3 Ga 5 O 12 nano-garnets. *Journal of Materials Chemistry*, *22*(27), 13788-13799.

[26] Inokuti, M., & Hirayama, F. (1965). Influence of energy transfer by the exchange mechanism on donor luminescence. *The journal of chemical physics*, *43*(6), 1978-1989.

[27] León-Luis, S. F., Rodríguez-Mendoza, U. R., Haro-González, P., Martín, I. R., & Lavín, V. (2012). Role of the host matrix on the thermal sensitivity of Er3+ luminescence in optical temperature sensors. *Sensors and Actuators B: Chemical*, *174*, 176-186.

[28] Cheng, Y., Gao, Y., Lin, H., Huang, F., & Wang, Y. (2018). Strategy design for ratiometric luminescence thermometry: circumventing the limitation of thermally coupled levels. *Journal of Materials Chemistry C*, *6*(28), 7462-7478.

[29] Xu, W., Gao, X., Zheng, L., Zhang, Z., & Cao, W. (2012). An optical temperature sensor based on the upconversion luminescence from Tm3+/Yb3+ codoped oxyfluoride glass ceramic. *Sensors and Actuators B: Chemical*, *173*, 250-253.

[30] Barnett, J. D., Block, S., & Piermarini, G. J. (1973). An optical fluorescence system for quantitative pressure measurement in the diamond-anvil cell. *Review of scientific instruments*, *44*(1), 1-9.

[31] Tröster, T. (2003). Optical studies of non-metallic compounds under pressure. *Handbook on the Physics and Chemistry of Rare Earths*, *33*, 515-589.

[32] Syassen, K. (2008). Ruby under pressure. *High Pressure Research*, *28*(2), 75-126.

[33] Hart, H. V., & Drickamer, H. G. (1965). Effect of high pressure on the lattice parameters of Al2O3. *The Journal of Chemical Physics*, *43*(7), 2265-2266.

[34] Finger, L. W., & Hazen, R. M. (1978). Crystal structure and compression of ruby to 46 kbar. *Journal of Applied Physics*, *49*(12), 5823-5826.

[35] McCumber, D. E., & Sturge, M. D. (1963). Linewidth and temperature shift of the R lines in ruby. *Journal of Applied Physics*, *34*(6), 1682-1684.

[36] Piermarini, G. J., Block, S., Barnett, J. D., & Forman, R. A. (1975). Calibration of the pressure dependence of the R 1 ruby fluorescence line to 195 kbar. *Journal of Applied Physics*, *46*(6), 2774-2780.

[37] Nakano, K., Akahama, Y., Ohishi, Y., & Kawamura, H. (2000). Ruby scale at low temperatures calibrated by the NaCl gauge: wavelength shift of ruby R1 fluorescence line at high pressure and low temperature. *Japanese Journal of Applied Physics*, *39*(3R), 1249.

[38] Wang, F. (2005). *Self-organization and stress in network glasses* (Doctoral dissertation, University of Cincinnati).

[39] Fukuda, T., & Chani, V. I. (Eds.). (2007). *Shaped crystals: growth by micro-pulling-down technique* (Vol. 8). Springer Science & Business Media.

[40] Yoshikawa, A., Nikl, M., Boulon, G., & Fukuda, T. (2007). Challenge and study for developing of novel single crystalline optical materials using micro-pulling-down method. *Optical Materials*, *30*(1), 6-10.

[41] Waeselmann, N. (2012). Structural transformations in complex perovskite-type relaxor and relaxor-based ferroelectrics at high pressures and temperatures.

[42] Dieke, G. H., Crosswhite, H. M., & Crosswhite, H. (1968). Spectra and energy levels of rare earth ions in crystals.

[43] Iffländer, R. (2001). *Solid-state lasers for materials processing: fundamental relations and technical realizations* (Vol. 77). Springer Science & Business Media.

[44] Carnall, W. T., Fields, P. R., & Rajnak, K. (1968). Electronic energy levels in the trivalent lanthanide aquo ions. I. Pr^{3+}, Nd^{3+}, Pm^{3+}, Sm^{3+}, Dy^{3+}, Ho^{3+}, Er^{3+}, and Tm^{3+}. *The Journal of Chemical Physics*, *49*(10), 4424-4442.

[45] Nekvasil, V. (1978). The crystal field for Nd^{3+} in garnets. *Physica status solidi (b)*, *87*(1), 317-323.

[46] Antic-Fidancev, E., Hölsä, J., Lastusaari, M., & Lupei, A. (2001). Dopant-host relationships in rare-earth oxides and garnets doped with trivalent rare-earth ions. *Physical Review B*, *64*(19), 195108.